Spaceborne infrared imagery for early detection and cause of Weddell Polynya openings

Céline Heuzé[1] and Adriano Lemos[1]

[1]Department of Earth Sciences, University of Gothenburg, Gothenburg, Sweden

Correspondence: Céline Heuzé (celine.heuze@gu.se)

Abstract. Knowing when sea ice will open is crucial for navigation and scientific deployments. This became painfully obvious when the Weddell Polynya, a large opening in the winter Southern Ocean sea ice, unexpectedly re-appeared in 2016 for the first time in forty years. With no warning, observations were limited to chance autonomous sensors, so the much-debated cause of the opening still cannot be determined accurately. We investigate here whether the signature of the vertical ocean motions or that of the leads, which ultimately re-open the polynya, are detectable in spaceborne infrared temperature. From the full historical sea ice concentration record, we find in fact 30 polynyas since 1980. Then, using the full time series of the spaceborne infrared Advanced Very High Resolution Radiometer, we determine that these events can be detected in the two weeks before the polynya opens as a reduction in the variance of the data. For the three commonly used T3b, T4 and T5 infrared brightness temperatures, the 15-day sum and 15-day standard deviation of their area-median and -maximum are systematically lower than the climatology when a polynya will open. Moreover, we find temporal oscillations in infrared brightness temperature that could indicate upwelling of warm water, but also changes of sign in T45 (band 4 – band 5) which could indicate a lead. We hence combine the spaceborne infrared data with atmospheric reanalysis, hydrographic mooring data and Sentinel-1 radar imagery and find that all events, including the 2017 Weddell Polynya, may be caused by both atmospheric divergence and oceanic upwelling.

1 Introduction

Global changes in the sea ice cover, of which the continuous decrease in summer Arctic sea ice since satellite observations began in the 1970s is the most dramatic example (Stocker et al., 2014; Notz and Stroeve, 2016), lead to a development in commercial exploitation of ice-infested waters in both hemispheres (Meier et al., 2014; Schillat et al., 2016). For planning purposes, early detection of sea ice opening is urgently needed. Polar researchers would also benefit from such product. In 2016, the most famous opening in the Antarctic sea ice, the Weddell Polynya (Carsey, 1980), re-appeared for the first time in forty years (Swart et al., 2018). Luckily, two autonomous profilers were drifting over the polynya region as it was opening (Campbell et al., 2019), but these are the only data ever collected during one of its openings. Early-warning, even if it is but a

few days, would allow for potentially re-routing autonomous sensors or nearby expeditions and hence obtaining such precious data.

Polynyas are large openings in the sea ice, in both hemispheres, located by the coast or in the open ocean (Morales Maqueda et al., 2004; Smith Jr et al., 2007). By suddenly exposing the comparatively warm ocean to the cold winter atmosphere, they have a large impact on the entire climate system: they modify the whole water column (Gordon, 1978), contribute to deep water formation (Martin and Cavalieri, 1989) and hence impact the global ocean circulation (Heuzé et al., 2015a), and may be responsible for the observed warming of the deepest waters (Zanowski et al., 2015). Moreover, the vertical motion of water that they trigger ventilates the deep ocean and brings nutrients up, making polynyas a biological hotspot (Smith Jr et al., 2007). The largest of them all, the Weddell Polynya or Maud Rise Polynya, opens in austral winter in the Weddell Sea sector of the Southern Ocean. Until 2016, it had been observed only once, at the beginning of the satellite era in winters 1974-1976, when it reached a maximum area of 350 000 km^2 (Carsey, 1980). Although there was no Weddell Polynya in the following 40 years, a "halo" of low sea ice concentration did regularly appear in the region (Lindsay et al., 2004; Smedsrud, 2005; de Steur et al., 2007), suggesting that the process that caused the polynya was still at play. The 1970s polynya has been extensively studied using models (e.g. Timmermann et al., 1999; Cheon et al., 2015; Cabré et al., 2017), but the exact, general-case opening process is still debated, owing to the lack of in-situ data. The many hypotheses fall into two broad categories:

- the atmospheric argument is based on relationships between the polynya and the strength or persistence of the Southern Annular Mode, the strength of the wind itself (e.g. Cheon et al., 2014; Francis et al., 2019; Campbell et al., 2019), or even on moisture transport (Francis et al., 2020);
- the oceanographic argument is two-fold: that the Maud Rise region is weakly stratified, hence prone to deep convection and polynya events (Kjellsson et al., 2015; Heuzé et al., 2015b; Wilson et al., 2019), and that the polynya opens when comparatively warm Circumpolar Deep Water is upwelled (Holland, 2001; Martin et al., 2013; Dufour et al., 2017; Cheon and Gordon, 2019).

The lack of in-situ data could be compensated by satellite-based observations. The most common method to monitor sea ice globally consists in daily estimates of sea ice concentration from passive radiometers (Spreen et al., 2008), mostly in the microwave region (e.g. AMSR-E highest frequency of 89 GHz, or wavelength of approx. 3 mm). Passive microwave remote sensing is also commonly used for the determination of sea ice age (e.g. Maslanik et al., 2007), a proxy for its thickness and salinity. Passive microwave remote sensing products have a relatively low horizontal resolution of the order of 3 km, so (active) Synthetic Aperture Radar (SAR) has become common for high resolution applications such as lead (e.g. Murashkin et al., 2018) or melt pond detection (Mäkynen et al., 2014), sea ice drift tracking (e.g. Demchev et al., 2017), classification (e.g. Aldenhoff et al., 2018) and especially thickness retrievals (e.g. Zhang et al., 2016). To the best of our knowledge, none of these methods has been used for detecting that sea ice is about to open. Moreover, SAR is a comparatively recent technology for sea ice observation, providing climate data only since the early 2000s (Drinkwater, 1998). In contrast, spaceborne infrared imagery has been used to monitor sea ice since the late 1970s from multi-mission satellites, which gives a higher-than-daily coverage and makes it a quite robust method (Comiso, 1991). Our hypothesis, based on our preliminary study (Heuzé and Aldenhoff,

2018), is that the upwelling and/or heat loss to the atmosphere caused by sea ice thinning prior to the Weddell Polynya opening is detectable in infrared data.

We here investigate whether spaceborne infrared imagery can be used to detect an upcoming re-opening of a polynya. We base our study on the Advanced Very High Resolution Radiometer Polar Pathfinder, provided by the National Oceanographic and Atmospheric Administration (Key et al., 2019). After detailing our processing in section 2, in particular the cloud masking, we start by verifying how many polynya events have occurred since records began (section 3.1) and their respective starting dates, using the "Bootstrap Sea Ice Concentrations from Nimbus-7 SMMR and DMSP SSM/I-SSMIS, Version 3.1" from the National Snow and Ice Data Center (Comiso, 2017). We then determine criteria on the infrared brightness bands that successfully detect all these events and minimise the amount of false positives (section 3.2). Finally, as the infrared time series can also show whether the polynya opened from a lead or from upwelling, we further investigate the events for which we have in-situ data in the vicinity, including the much-debated 2017 Weddell Polynya (section 4).

2 Data and Methods

2.1 Data

In the interest of readability, we now indicate only the key characteristics of the data used for this study. The reader is encouraged to consult the corresponding data description papers that we cite. In this study, we first determine the dates of past polynya events using the daily product "Bootstrap Sea Ice Concentrations from Nimbus-7 SMMR and DMSP SSM/I-SSMIS, Version 3.1" at 25 km resolution from the National Snow and Ice Data Center, and available continuously since 1 November 1978 (Comiso, 2017, dataset doi: 10.5067/7Q8HCCWS4I0R).

We then study these events using spaceborne infrared data, validated against in-situ hydrographic and atmospheric reanalysis data, but also SAR imagery. Our region of interest (Fig. 1), hereafter referred to as “the polynya-prone region”, is the fixed 778 000 km^2 area that lies over the topographic feature Maud Rise, in the eastern Weddell Sea sector of the Southern Ocean (longitude 6° W to 12° E; latitude 68° S to 60° S), where polynyas and halos have been consistently reported in the literature (e.g. Beckmann et al., 2001; de Steur et al., 2007; Campbell et al., 2019).

The spaceborne infrared data come from the Advanced Very High Resolution Radiometer (AVHRR) Polar Pathfinder or APP, provided by the National Oceanographic and Atmospheric Administration (Key et al., 2019, dataset doi: 10.25921/X2X1-JR34). It provides twice-daily, 5 km gridded composites of all available AVHRR infrared brightness temperature data since 1982. We use only the ones acquired in the 6h interval around 2 AM local solar time. The three bands that we use are commonly referred to as T3b (wavelength of 3740 nm), T4 (10800 nm) and T5 (12000 nm). Over the polynya-prone region, the APP data contain 90 000 grid cells.

To try and explain which oceanic or atmospheric processes are responsible for the infrared brightness temperature signals, we use the hourly 2 m temperature and 10 m horizontal wind components u and v from the European Centre for Medium-Range Weather Forecasts ERA5 hourly reanalysis, provided on a 0.25° grid (dataset doi: 10.24381/cds.adbb2d47). Hydrographic data come from three moorings deployed along the Prime Meridian by the Alfred Wegener Institute, named AWI229 (Fahrbach

and Rohardt, 2012a; Rohardt and Boebel, 2019, dataset doi: 10.1594/PANGAEA.793018 and 10.1594/PANGAEA.898781), AWI 230 (Fahrbach and Rohardt, 2012b, c, dataset doi: 10.1594/PANGAEA.793080 and 10.1594/PANGAEA.793082) and AWI 231 (Fahrbach and Rohardt, 2012d, dataset doi: 10.1594/PANGAEA.793089). Each mooring deployment has different characteristics, but they all measure temperature, salinity, pressure, and current velocity (not used here) at up to 15 irregularly spaced depth levels, every 15 min, for on average two years. The earliest deployments were in April 1996, and the program continues to date.

Finally, to find the signature of open water / new ice, we use C-Band HH backscatter information from four Sentinel-1 SAR images in the extra-wide swath mode (approx. 40 m resolution) provided by the European Space Agency / Copernicus. The images were acquired on 18, 23, 26, and 30 August 2017 around 20 UTC, i.e. 3h before the APP compositing begins. We use only the HH polarisation, as we do not perform a detailed analysis but rather a qualitative assessment of sea ice conditions.

2.2 Cloud masking of APP data

Clouds are a known issue for AVHRR data, especially in polar regions (e.g. Drinkwater, 1998). The first cloud filters adapted to the polar regions were designed by Yamanouchi et al. (1987), which imposed criteria on T4, T34 (T3b minus T4) and T45 (T4 minus T5) to detect thick, high and thin clouds, respectively. Saunders and Kriebel (1988) added a geographical/texture perspective, imposing criteria on 3 by 3 pixel areas, while Key and Barry (1989) added a temporal perspective, comparing each pixel from day to day. But these filters did not perform as well as expected, and we had to wait until Vincent et al. (2008) for extra criteria on T45 that can detect ice fog, and more recently Vincent (2018) to detect dust.

We aim to create a system that can work on individual images independently, so the approach of Key and Barry (1989) is not adapted. Likewise, Saunders and Kriebel (1988) is mostly based on day-time images, so not for us. As detailed in Appendix A, after validation using the reference cloud mask MYD35_L2 v6.1 (Ackerman et al., 2017, dataset doi:10.5067/MODIS/MYD35_L2.006) over the period 4 July 2002 - 31 December 2018 that is common to both products, we chose to use the following three criteria to detect clouds (example on Fig. 1):

- T4 $<$ 245 K (indigo, Yamanouchi et al., 1987);
- |T34| $>$ 1.5 K (green, after Yamanouchi et al., 1987, see appendix A);
- T45 $<$ 0 K or T45 $>$ 2 K (yellow, Vincent et al., 2008; Vincent, 2018).

As shown on Fig. 1 and in Appendix A, these criteria are not perfect but they are powerful enough to detect most of the clouds. On average, only 14% of the cloud pixels are missed, but 15% of the pixels are also wrongly eliminated as cloudy even though they are clear. We strongly suspect that this is caused by the difference in acquisition time of the images used by each product, but could not verify this as APP is directly available as a composite instead of distinct images. Moreover, leads and polynyas generate a large heat and moisture flux (e.g. Cheon et al., 2014), so we need a cloud mask that is not so sensitive that it would mask the leads and polynyas and prevent us from detecting them. As our cloud masking is based on published literature and that cloud masking is not the topic of this paper, any further study of this question would be beyond the scope of this paper.

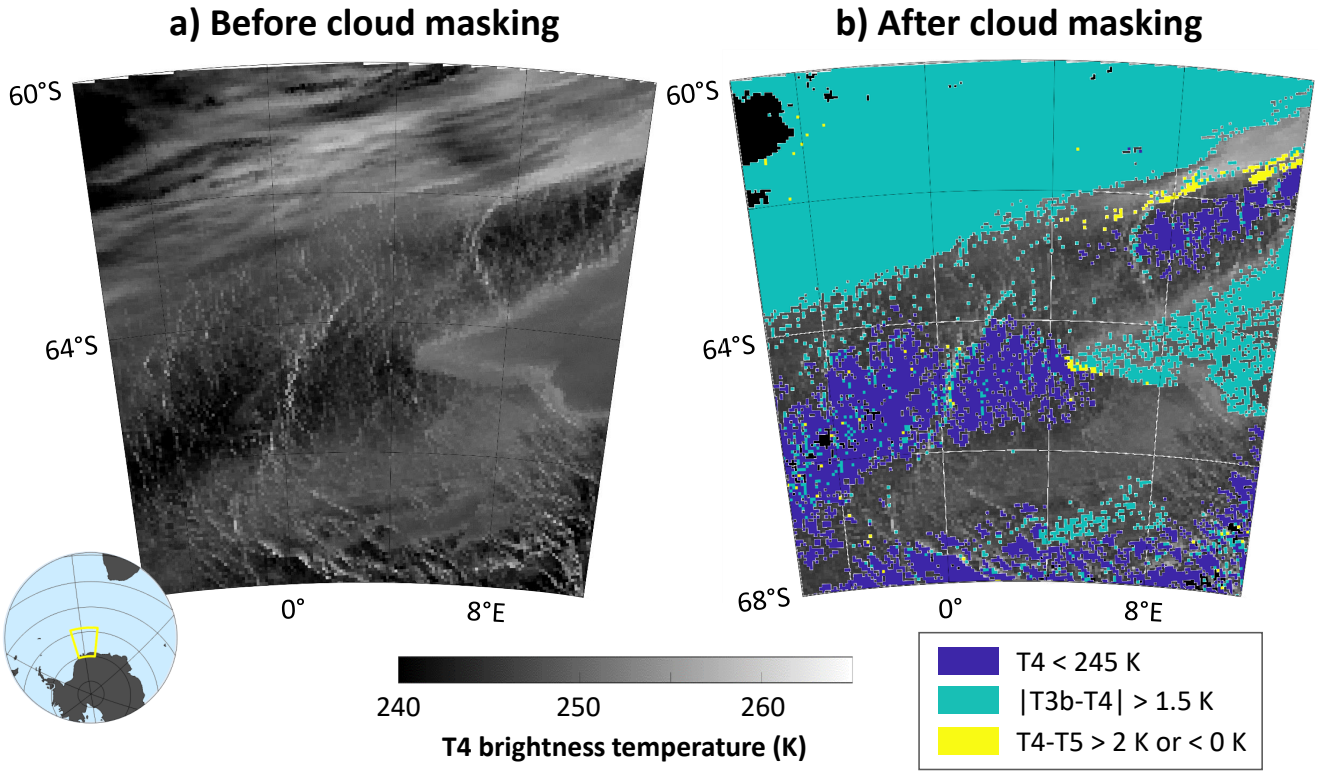

Figure 1. Infrared brightness temperature T4 from APP (provided by NOAA, Key et al., 2019) on 13 August 2009 before (a) and after (b) cloud masking. Colours indicate the different masking criteria on T4 (Yamanouchi et al., 1987, indigo), T34 (as detailed in appendix A, modified from Yamanouchi et al., 1987, green), and T45 (Vincent et al., 2008; Vincent, 2018, yellow). Insert indicates the location of the two images.

Any pixel that meets any of the three criteria listed above is set to NaN in all three bands T3b, T4 and T5 for our calculations. The polynya events and the days leading to them that we study in this paper have a similar amount of cloud free pixels to any of the non-polynya years in the series (supp. Fig. B1).

2.3 Methods

There are many criteria to detect a polynya based on sea ice concentration thresholds (see Mohrmann et al., 2021, and references therein). In section 3.1, we detect polynyas by applying already published methods based on sea ice concentration threshold on each pixel and on the area-average. We show only the three different thresholds used by Gloersen et al. (1992); Gordon et al. (2007); Campbell et al. (2019), but we tested and visually assessed, using the authors' experience, each option between 15 and 100% on the single-pixel sea ice concentration. We compute the polynya area by detecting the contour of the enclosed area with a sea ice concentration lower than the specific threshold (see codes if needed). An event is defined as an uninterrupted series

of consecutive days with sea ice under that threshold (60% in this study); if there is a day with higher sea ice concentration in between, a new event is created. We will show in section 3.1 that there has been more than 20 polynya events over the last 40 years covered by the sea ice concentration product, and use the polynya events here detected to determine the characteristics of the infrared brightness temperature in the days leading to each event.

The aim of our work is to eventually produce an automatic system that would be scanning the polynya-prone region, so we do not track individual polynyas and instead analyse the infrared brightness temperature time series over the whole region in section 3.2. We also computed daily anomalies of these infrared brightness temperatures relative to daily climatological values over the whole 38 year period covered by APP. For each day from 1982 to 2019, we produce time series of the geographical median, standard deviation, minimum and maximum infrared brightness temperature over the polynya-prone region for each band.

Finally, the atmospheric and hydrographic data used in section 4 are directly studied without further processing, except for the wind components. We produced for each polynya event a time series of so-called curl of the wind. We cannot compute the wind stress curl per se, as we lack the drag coefficient, which will anyway change depending on whether the polynya is open or close. So instead, we use a similar method as e.g. Petty et al. (2016) and work with the curl of the wind components u and v:

$$curl = \frac{\partial v}{\partial x} - \frac{\partial u}{\partial y}. \quad (1)$$

We are not studying the actual values of that curl, only whether it is positive (suggesting divergence that could open a lead) or negative (suggesting an upwelling, Marshall and Plumb, 2016).

3 Results: an infrared-based criterion valid for all polynya events

3.1 Polynya dates

We start by determining the dates of the polynya events that we want to further study according to three traditional criteria: sea ice concentration (SIC) minimum over the region lower than 15% (after e.g. Gloersen et al., 1992, black, Fig. 2) or lower than 60% (Campbell et al., 2019, blue), and average SIC lower than 92% (Gordon et al., 2007, red). As explained previously, we study the fixed "polynya-prone" region of longitudes 6°W to 12°E and latitudes 68°S to 60°S. We limit ourselves to the period 1st July to 31st October. As noted by Campbell et al. (2019) already, these methods return qualitatively similar results; it is only the number of days that differs for each criterion. They all agree there was some polynya activity in the late 1980s - early 1990s and in the early 2000s, the so-called Maud Rise halo already studied notably by de Steur et al. (2007). Then, the region was rather quiet until the widely reported 2016-2017 return of the polynya (Swart et al., 2018).

The 60% criterion represented by the blue line probably includes late freeze-up or early melt events. The actual method used by Campbell et al. (2019) does not use fixed dates for winter, but instead limits itself to the period that starts one week after the first 90% SIC and finishes one week before the last 90%. For consistency with the other two methods, we used fixed winter dates for all criteria. We then visually checked the individual images to separate such late freeze-up / early melt from the actual

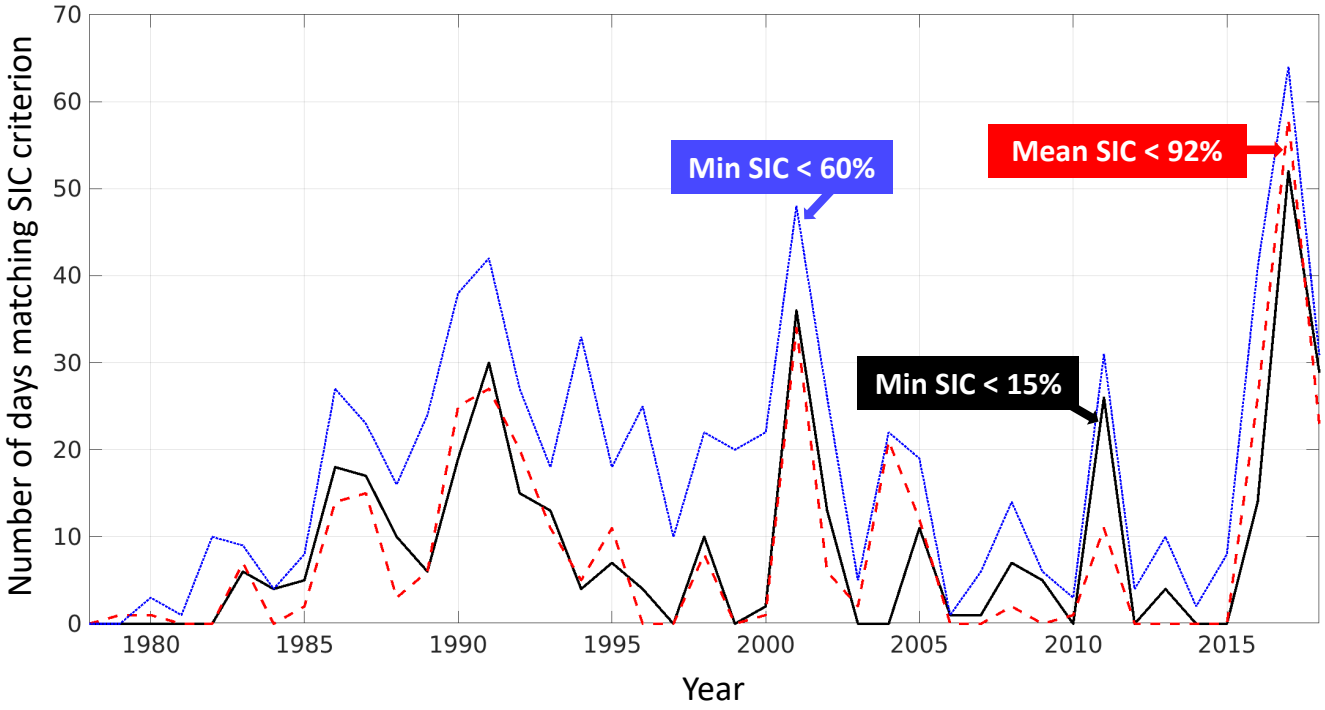

Figure 2. For each year of the NSIDC sea ice time series (1978-2018), number of days between 1st July and 31st October with a polynya according to the three most common criteria in the literature: black, minimum sea ice concentration (SIC) lower than 15% (e.g. Gloersen et al., 1992); blue, minimum sea ice concentration lower than 60% (Campbell et al., 2019); red, average sea ice concentration over the (fixed) polynya-prone region lower than 92% (after Gordon et al., 2007).

polynya events. This confirmed that although most sensitive, the 60% criterion used by Campbell et al. (2019) performs best (not shown).

The characteristics of the events thus detected are given in appendix table B1. We have 24 events over 11 years, which yields 30 polynyas because 5 events have two to four polynyas in the region simultaneously. Note that all durations make the polynya disappear on 1st November because of our end date criterion.

These 30 polynyas open at key locations in the region (Fig. 3). The maximum number of polynyas opening at the same grid cell, nine, is on the north-east flank of Maud Rise, with most of the others opening over Maud Rise or on its south-west flank. The central role of Maud Rise as shown by Holland (2001) is obvious. There is also a non-negligible number of grid cells in the southern part of our region with at least one opening. Unlike in models (e.g. Martin et al., 2013), Fig. 3 shows no opening over the open ocean.

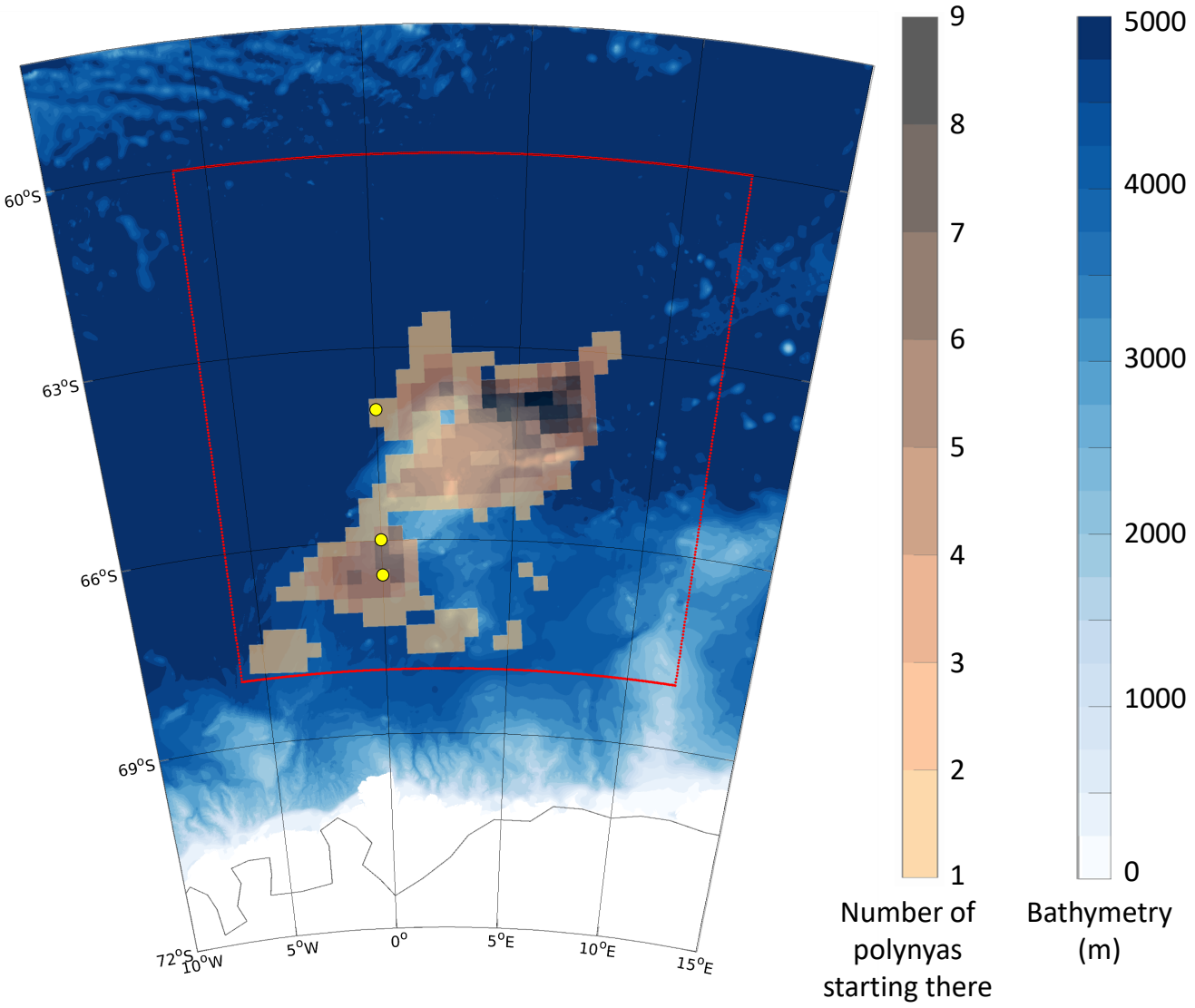

Figure 3. Out of the 30 polynyas detected, how many start at each location (transparent shading). Background: bathymetry of the region from GEBCO Compilation Group (2019). Red contours indicate the polynya-prone region studied in this manuscript. Yellow dots mark the location of the three moorings used in section 4: AWI229 (north), AWI230 (middle) and AWI231 (south).

3.2 Infrared-based early detection criteria

In the previous section, we determined the dates of 24 polynya events (giving 30 actual polynyas) from sea ice data dating back to 1978. We now investigate, in the timeseries of infrared brightness temperature from APP, whether all these events share something in common, especially in the 15 days leading up to the event. We present the 30 days prior to the events in

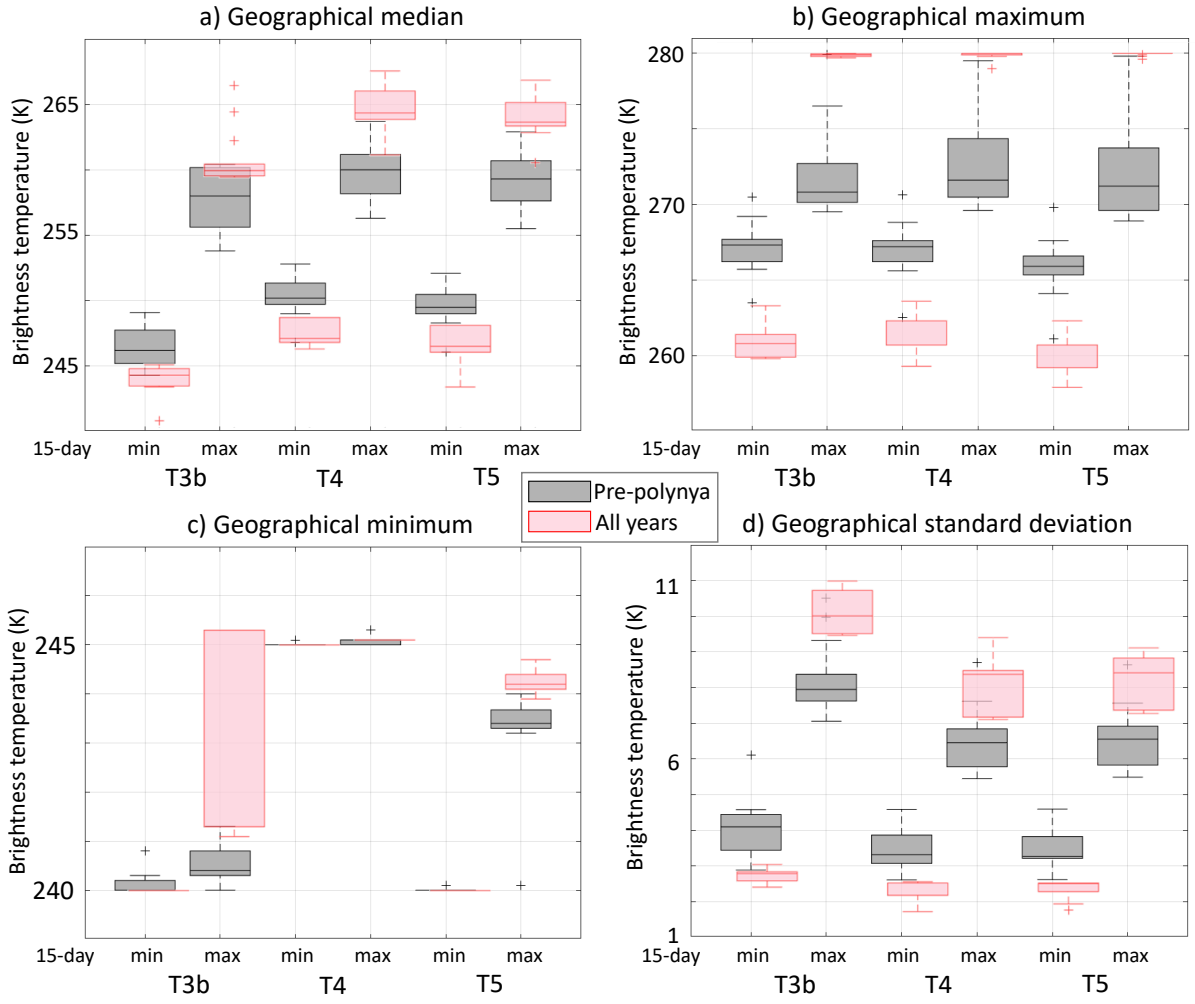

Figure 4. Over the polynya-prone region, for all bands, whisker plot of the minimum (x-axis) and maximum (y-axis) infrared brightness temperature over the time period from 15 days before the polynya opens until the day of opening of the geographical median (a), maximum (b), minimum (c) and standard deviation (d). Grey colours show the values of the years where a polynya opens; pink, for the same dates in all years.

section 4 but we found that for the current purpose, 15 days are enough. As explained in the Methods section, this "something in common" needs to be easily detectable by a crude automatised system, hence we computed basic single-image properties over the entire polynya-prone region: the geographical median, minimum, maximum and standard deviation. We analyse the range of their values in the 15 days leading to the event and compare them to years with no polynyas (Fig. 4).

We want to find a criterion that would not only robustly detect a polynya, but also not flag any false positive. Fig. 4 shows that finding a simple threshold criterion will not be possible. For all geographical statistics and all bands, the range of the

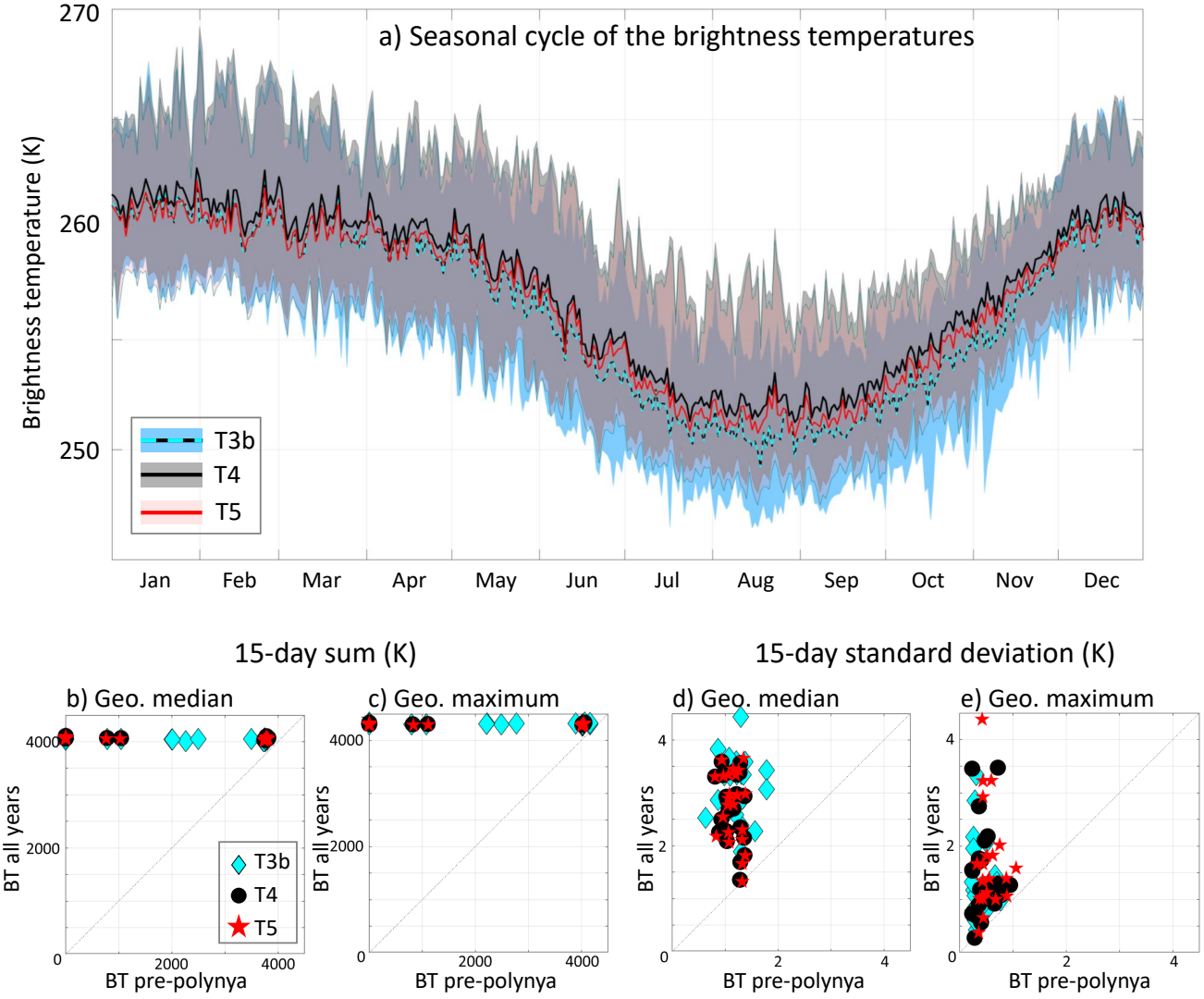

Figure 5. For the three bands, a) 1982-2019 median (thick line) and 10 to 90 percentiles (shading) infrared brightness temperature value for each day of year. b) to d) demonstrate the narrow range of the infrared brightness temperature (BT) statistics over the 15 days leading to each polynya (x-axis) compared to that on the same date in all years (y-axis): 15-day sum of the geographical b) median and c) maximum; 15-day standard deviation of the geographical d) median and e) maximum. One point per polynya event: cyan diamonds for the temperature band T3b; black circle for T4; red star for T5. Thin black line is the unit line.

185 polynya values (grey on Fig. 4) is contained in the range of the years with no polynya (pink): the 15-day minima are larger when there is a polynya; the maxima, lower. We find the same results when looking at T34, T45 and T35, as well as all bands' anomalies (not shown).

One reason for the impossibility of finding an absolute threshold may be the seasonal cycle both in infrared brightness temperature and in anomalies (Fig. 5a). Polynyas are detected any time between early July and late October (supp Table B1). It is thus not surprising that a threshold that would successfully detect a polynya in August, when the brightness temperature is at its minimum but anomalies in T4 and T5 are largest, would fail in October as the temperature is higher and anomalies lower (Fig. 5a).

Instead, the narrower range of values during a polynya shown on Fig. 4 suggests that a criterion based on the persistance of values may be more adapted. Indeed, we find that years with polynyas have systematically lower 15-day sum or 15-day standard deviation than their non-polynya counterparts, in any band, with any geographical statistics although it is clearest with the geographical median and maximum (Fig 5 b to d). We find the same result when using the overall climatology instead of only the years with no polynya. We find no false positive.

In summary, a polynya is going to open if the 15-day sum or 15-day standard deviation of its geographical median or maximum over the polynya-prone region is lower than the 15-day sum or standard deviation produced using the climatology at the same date. See also Fig. 6 for a summary in flowchart form. Such low variability could be atmospheric driven, the result of a blocking-event. Studying the large scale atmosphere dynamics is beyond the scope of this paper, and a brief comparison of the 2-m air temperature over the polynya-prone region in the 15 days leading to each event (supp. Fig. B2) shows a lot of variability in the atmosphere. That is, pronounced changes in temperature for each event (e.g. up to 25° increase in 2 days for the first event), and no consistency among the events in magnitude and sign of the variations. The blocking explanation seems unlikely and would anyway be in opposition to the latest research on the atmospheric drivers of the Weddell polynya (see e.g. Francis et al., 2019, and references therein). It is thus more likely that the low-variability in infrared brightness temperature is the result of latent heat exchanges in the ocean-ice-atmosphere system as sea ice melts and refreezes.

We have determined a method based on infrared brightness temperature data to detect a polynya before it opens. Can we extract more information out of these infrared brightness temperatures? For example, an answer to the much debated "why did the polynya open"? One option is the difference between bands T4 (most adapted to ice) and T5 (most adapted to open ocean) or T45, where $T45 < 0$ means lead (Vincent et al., 2008). Unfortunately, out of the 24 events, all of them (see e.g. Fig. 7a) had a minimum T45 lower than 0 in the 14 days before the event. This would mean that all of them had a lead somewhere in the polynya-prone region, which is possible. The other option is that, as hypothesised by Heuzé and Aldenhoff (2018), oscillations in the infrared brightness temperature in the days before the polynya might reflect oceanic convective movements. The argument is that as the warm water is being upwelled, more heat is going through the ice; same as the ice thins, melted from below by that warm water. But likewise, all polynya events exhibit such oscillations, albeit with a frequency varying from 1 to 3 days depending on the band and event (see e.g. Fig. 7b and c). In conclusion, we cannot determine the cause of the polynya opening from the infrared images alone. In the next section, we investigate this further, using in-situ validation data.

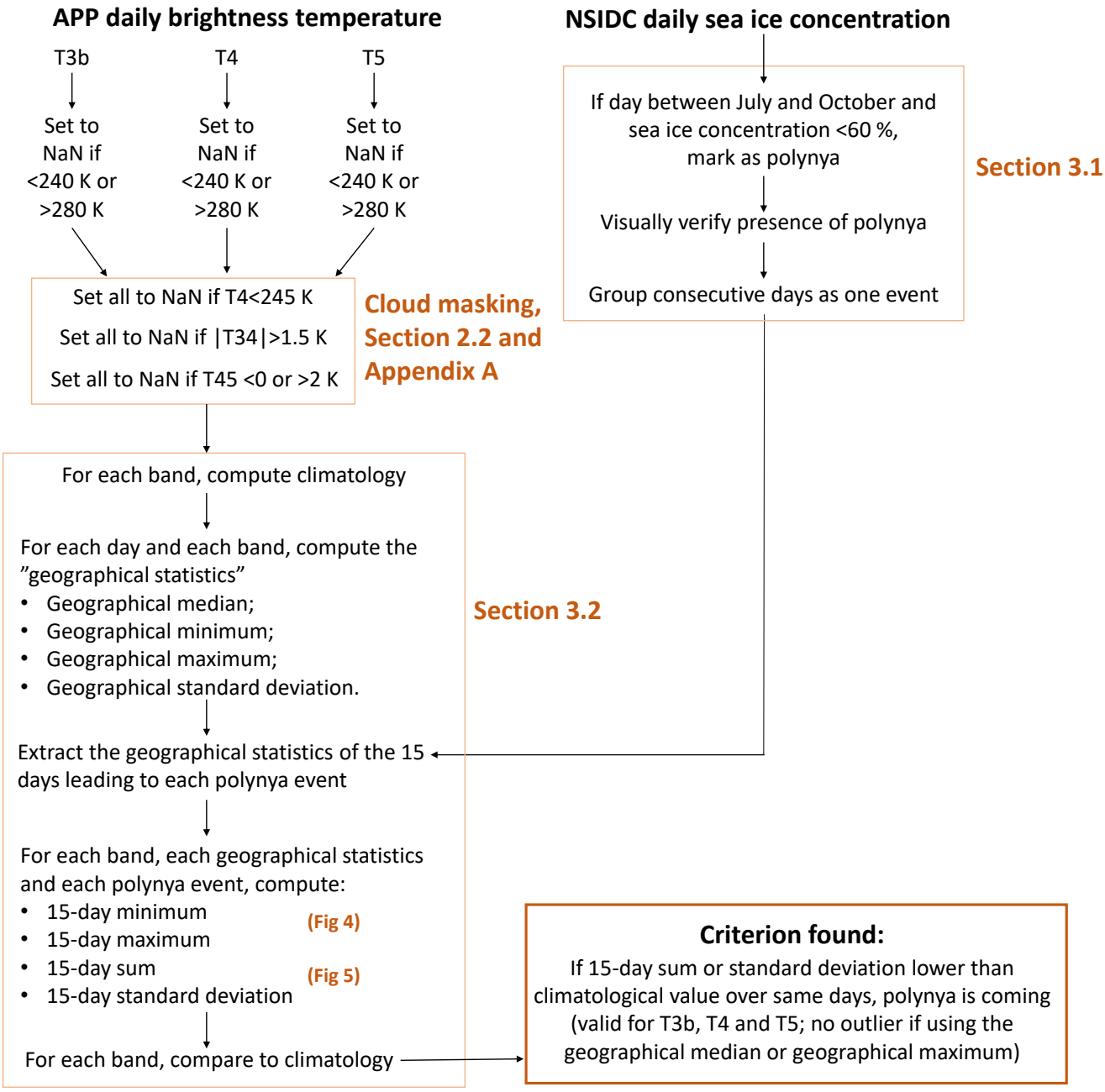

Figure 6. Flow chart summarising our methods and the findings of section 3.2.

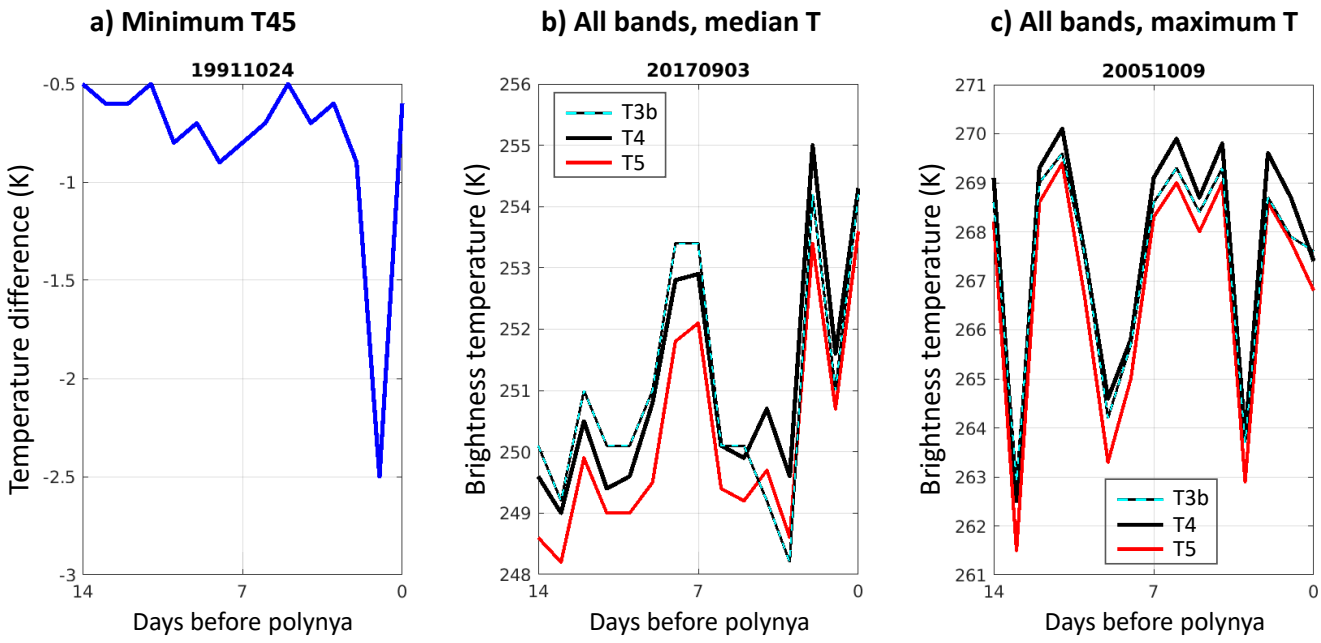

Figure 7. Example time series of geographical a) minimum infrared brightness temperature difference T45 (T4 minus T5); b) median and c) maximum infrared brightness temperature for all three bands, over the 14 days leading to the polynya event (date of the event in the panel title). For b) and c), thin dashed cyan line indicates T3b, thick black line T4, and red line T5.

4 Discussion: can infrared brightness temperature reveal why the polynyas open?

There are two ways to open a polynya (Morales Maqueda et al., 2004):

- sensible heat / open ocean polynyas form when the sea ice is melted from below by the ocean. It requires that a comparatively warm water mass is upwelled, which should be visible in oceanic mooring data. A negative curl of the wind would indicate Ekman pumping, i.e. that the atmosphere is favourable to upwelling. Finally, positive air temperatures before the opening would contribute to the melting;
- latent heat / coastal polynyas in contrast form when the sea ice is pushed away by the wind. A positive curl of the wind would indicate such divergence.

From the infrared images, both mechanisms are possible: the oscillations in brightness temperature suggest an upwelling of warm water, but could also warm air intrusions (warm air discussed for the 2017 Weddell Polynya by Francis et al., 2020). Simultaneously a negative T45 suggests that leads open. We hence now augment our spaceborne infrared data with atmospheric and hydrographic data for clarification.

The data coverage for the atmosphere is much better than for the hydrography, so we start with the atmosphere. We first investigate whether the air temperature would be high enough to melt the sea ice from above. Unfortunately, we do not know what the melting point of the sea ice is for each event, as we do not know the salinity of the sea ice or that of its snow layer; snow layer whose thickness is unknown as well. Nandan et al. (2017) puts an upper limit to 20 g/kg, which yields a freezing temperature of -1.1 °C (IOC, SCOR and IAPSO, 2010), and 0 °C if the sea ice is old and/or the snow layer fresh. Out of the 30 polynyas, 15 reach either of these freezing temperatures (supplementary Fig. B2). The main caveat here though is that the air temperatures are not given at the surface of the ice, but at 2 m height where it may be colder. All that we can say then is that three polynya events are colder than or around -10 °C over the entire 15-day period that preceeds the polynya opening, but for all the others it might have been warm enough to melt the sea ice.

The air temperature data alone could not shed light on the process responsible for the opening of the polynya; can the wind data deliver more conclusive results? The curl of the wind at the location of the individual 30 polynyas (listed in Table B1) alternates between negative and positive values for all polynyas (supp Fig. B3, negative curl / upwelling is blue, positive curl / divergence is red). That is, all polynyas have been preceded by both upwelling-prone and divergent winds. Note that the required timing is unclear: for divergence, e.g. Francis et al. (2019) says that it can open the ice within 12 hours, but to the best of our knowledge, no such specific value has been published for the upwelling. All that we can conclude for now then is that the atmospheric reanalysis data did not provide a satisfactory discrimination.

We hence finish this paper with a more in-depth analysis of the individual polynya events for which we have mooring data in the vicinity. Five mooring deployments coincide with a polynya event: one mooring (230-2) for 1999, three (229-5, 230-4, 231-5) for 2004, and one (229-13) for 2017. We want to determine 1) whether we see in the mooring data upwelling of the comparatively warm and salty Circumpolar Deep Water (CDW), and 2) whether such upwelling is in sync with the infrared brightness temperature oscillations. Unfortunately, for four out of five deployments, we are limited in the top 500 m to one

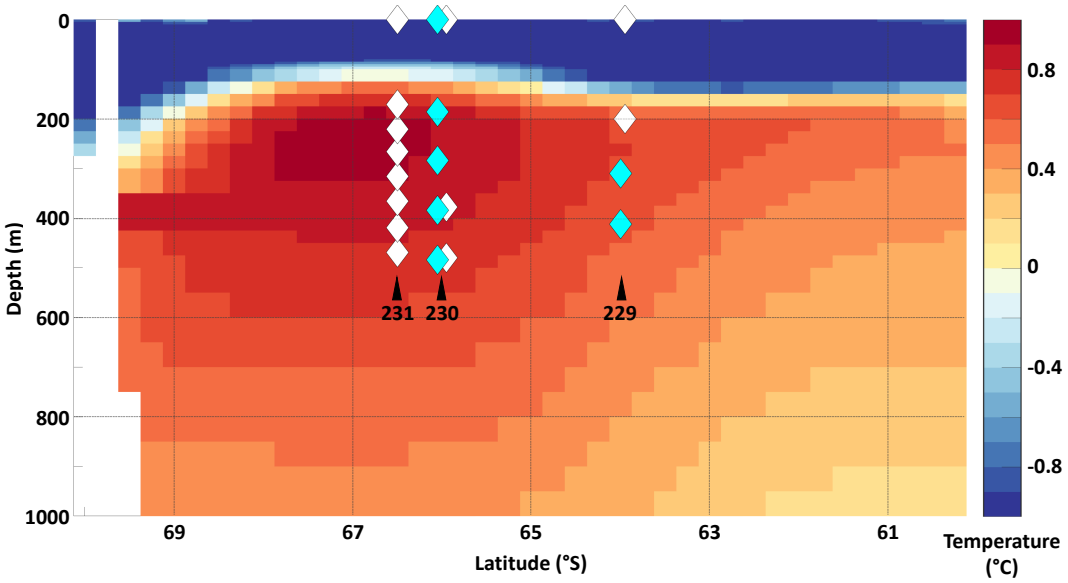

Figure 8. Climatological temperature along the Prime Meridian, from Locarnini et al. (2018), showing the comparatively warm Circumpolar Deep Water in red. The diamonds indicate the location of the mooring sensors used for our analysis; for moorings 229 and 230, white indicates the older deployment (229-5, in 2002-2005, and 230-2, in 1999-2000) and cyan, the more recent one (229-13, in 2016-2019, and 230-4, 2002-2005); for mooring 231, only deployment 231-5 (2002-2005) could be used here. Salinity section available as supplementary figure B4.

sensor at the surface and all the others in the CDW (Fig. 8 and supp. Fig. B4). We lack sensors in the top 100 m. Moreover, the surface sensor often had only temperature data, not salinity, and in the case of 229-13 for the 2017 polynya, there was no surface sensor data available. All we can study are variations in the CDW, both the suspected heaving of its core (Dufour et al., 2017) or its cooling as convection begins (Gordon, 1978). As sensors at the same depth returned different values but similar variability (not shown), we will not comment on the mooring values per se but only on their changes. To improve readability, as the three events present the same characteristics, we discuss here only 2017 but provide in the appendix the figures for 1999 (supp Fig. B5) and 2004 (supp Fig. B6).

In agreement with section 3.2, from 22 days before the 2017 event, the time series of the geographical median shows little variability, in all bands (Fig. 9a). There may be an anticorrelation with the hydrographic data at 310 m and 410 m depth (Fig. 9d, e), with a more marked increase in infrared brightness temperature as the water at depth becomes colder and fresher (first grey band, 16 days before), but this relationship is not significant. The alternance seen in the mooring data between cold/fresh and warm/salty along with changes in their variability does suggest that vertical movements are taking place, so we cannot reject the upwelling theory. Over the same period, divergent winds (red) blow and T45 decreases (Fig. 9b, c), so we cannot reject the lead theory either. Complementing our interpretation with high resolution Sentinel-1 SAR images, a qualitative analysis reveals that over that same period the ice is closed. Five days later, or 11 days before the event, there are leads all around

the area on the SAR image. One can imagine that the surface cooling resulting from the lead opening may have been strong enough to initiate convection, which would explain the apparent warming at 310 and 410 m. Note that the mooring is 2.5° to the west of the SAR image; the motion in the water column at the mooring location may therefore also be indicative of horizontal advection in response to more local upwelling at the exact location of the lead. We see that three days later, i.e. 8 days before the polynya, the leads have refrozen, so it is more likely is that the convection started as the ice formed again and ejected brine. The convection would bring down the cooled water from the surface to 310, 410 m depth, hence their cooling (as observed in reality and in models, Gordon, 1978; Smith Jr et al., 2007; Martin et al., 2013; Cheon and Gordon, 2019). And although we lack images between 8 and 4 days before the polynya, the fact that new freshly-refrozen leads appeared closer to the centre of the polynya area suggest that the ice opened again. In conclusion, the ice was very dynamic in 2017, with multiple openings and closing of leads potentially initiating oceanic convection.

In summary, our results agree with both the oceanographic (von Schuckmann et al., 2019; Cheon and Gordon, 2019) and the atmospheric (Francis et al., 2019; Campbell et al., 2019) arguments. The mooring data show a signal that may be that of upwelling, and wind-induced leads are visible on SAR images. That is, the Maud Rise polynya presents the characteristics of both a sensible and latent heat polynya. Such a phenomenon has in fact been observed recently in a polynya off Alaska, and dubbed "hybrid polynya" (Hirano et al., 2016). Maybe there has been no consensus in forty years because the Weddell Polynya is a hybrid polynya too.

5 Conclusions

The aim of this paper was to determine criteria on 38 years of spaceborne infrared imagery (APP) to detect an upcoming reopening of the Weddell Polynya. Using the NSIDC/Comiso Bootstrap sea ice concentration, we first generated a time series of past polynya events over Maud Rise and obtained 24 events since 1980, or 30 polynyas as some days had several polynyas opened simultaneously (Fig 2). The widely accepted narrative is that there had been no polynya in the Weddell Sea since "the" Weddell Polynya of 1974-1976 when the polynya unexpectedly re-opened in 2016 (e.g. Swart et al., 2018). Yet, our study is but one of many that found once again that there has in fact been many polynyas / halos in the region in the forty years in between (e.g. Lindsay et al., 2004; Smedsrud, 2005; de Steur et al., 2007; Campbell et al., 2019).

Although no absolute infrared brightness temperature threshold criterion could be found, all geographical statistics exhibit a reduced variability in the two weeks leading to any of these events compared to the same date in the rest of the dataset and in the climatology. The 15-day sum and 15-day standard deviation, in particular of the geographical median and maximum, successfully detected the events without finding false positives. The next step would be to check whether these criteria are still valid for other Antarctic open ocean polynyas, but also coastal polynyas (e.g. the Amundsen Sea Polynya Randall-Goodwin et al., 2015) or even Arctic polynyas (e.g. North Water and North Greenland polynyas, Preußer et al., 2015; Ludwig et al., 2019).

Finally, we investigated whether spaceborne infrared data could be used to answer the forty-year old debate: is it the ocean or the atmosphere that causes the Weddell Polynya to open? Using the infrared data combined with atmospheric reanalysis,

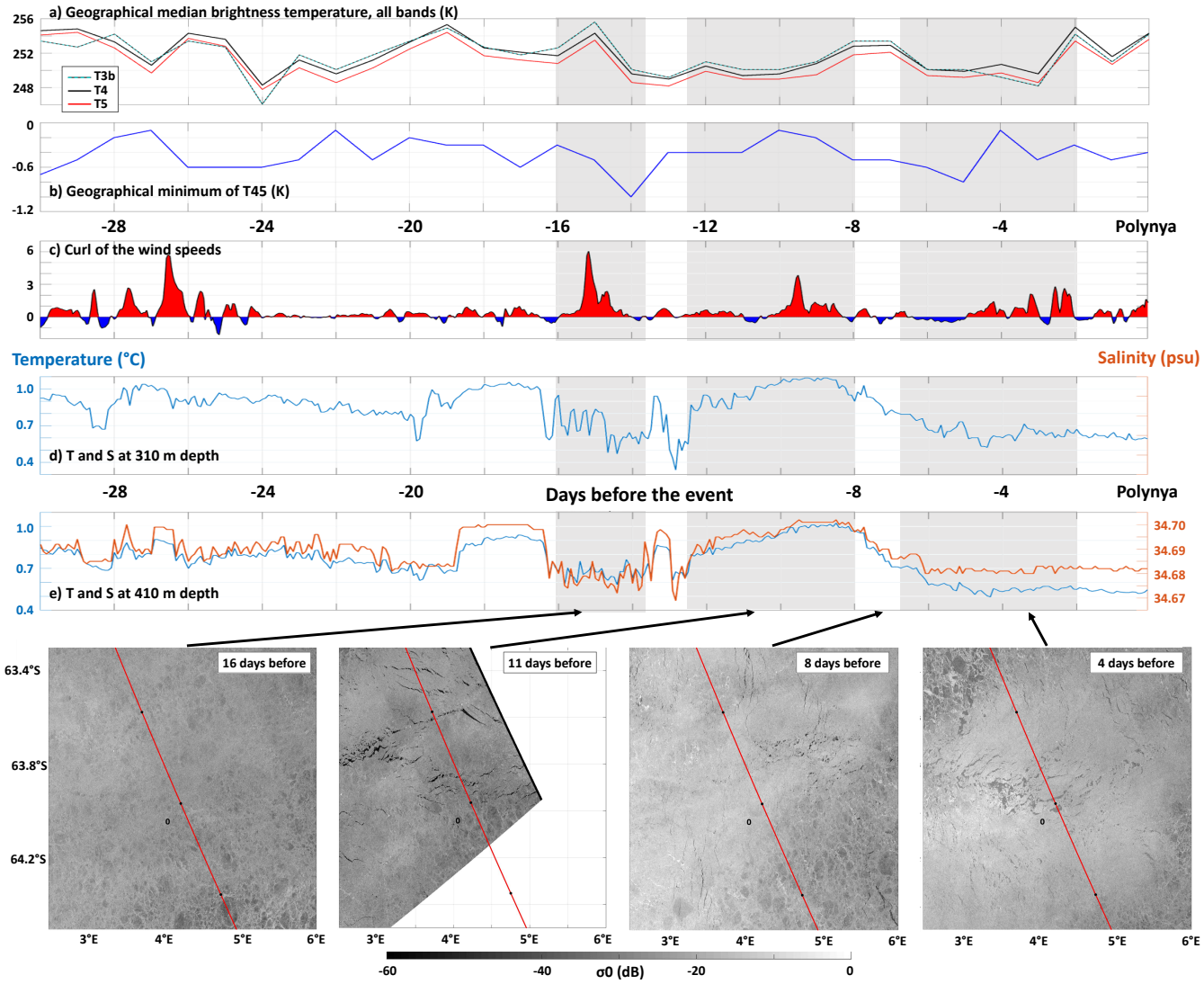

Figure 9. Conditions in the 30 days leading to the 3 September 2017 polynya. First, for the infrared criteria from section 3.2: a) geographical median over the polynya-prone region for the infrared brightness temperature band T3b (cyan), T4 (thick black) and T5 (red); b) geographical minimum over the polynya-prone region of the brightness temperature difference T45 (T4 minus T5). c) curl of the wind speeds as in supp Fig. B3. Temperature (blue) and salinity (orange) timeseries from mooring 229-13 located at 64°S, 0°E (see Fig. 8) at 310 (d), and 410 (e) m depth. Finally, Sentinel-1 images for four of these days, captured around 19 local time; observe the dark streaks made by leads. Red line indicates constant incidence angle; 0, the centre of the polynya region. Grey boxes in the background highlight the time periods discussed in the text. [Contains Sentinel-1 data, August 2017]

mooring hydrographic time series and even Sentinel-1 SAR imagery, we found evidence of both (Fig. 9). We found signatures that may be that of warm water upwelling and deep convection (e.g. Holland, 2001; Martin et al., 2013; Dufour et al., 2017;

Cheon and Gordon, 2019) but also of wind-driven lead opening (e.g. Gordon et al., 2007; Cheon et al., 2014; Campbell et al., 2019; Francis et al., 2019). This suggests that the Weddell Polynya may be a hybrid one, as happens for some Arctic polynyas (Hirano et al., 2016).

This study proved the crucial role of freely available high resolution products for the polar regions, but it would also not have been possible without continuous observation programs, both in space (AVHRR) and at sea (moorings). These must be maintained, as long time series are crucial not just for statistical exercises like here, but also to monitor climate change in the fast-changing polar regions (Stocker et al., 2014).

Code availability. Codes available at https://github.com/cheuze/Polynya_EGU_TC

Data availability. Sea ice data freely available online at https://nsidc.org/data/nsidc-0079.
APP infrared data freely available at https://www.ncei.noaa.gov/data/avhrr-polar-pathfinder/access.
ERA5 data freely available at https://cds.climate.copernicus.eu/cdsapp/dataset/reanalysis-era5-single-levels.
Mooring data freely available on PANGAEA at https://doi.pangaea.de/10.1594/PANGAEA.[dataset numbers in reference list].
Sentinel-1 data freely available at https://scihub.copernicus.eu/

Appendix A: Validation of the cloud masking

In section 2.2, we detect cloud pixels using the infrared brightness temperature thresholds of Yamanouchi et al. (1987), Vincent et al. (2008), and Vincent (2018). We here verify their methods using the Level 2 MODIS Cloud Mask product MYD35_L2 v6.1 (Ackerman et al., 2017, product DOI:10.5067/MODIS/MYD35_L2.006), obtained from https://search.earthdata.nasa.gov/ (last accessed 5 January 2021).

We obtained all MYD35_L2 granules available from 4 July 2002, when the product was first available, to 31 December 2018, over the region in the latitude range 68°S to 60°S and in the longitude range 6°W to 12°E, totalling nearly 65 000 granules. Latitudes and longitudes were available from the matching geolocation files (MYD03). For comparison with the APP data analysed here, we kept only the granules that were collected between three hours before and three hours after 2 am local solar time. In that time interval, we kept only the granules where the cloud mask was determined (first bit field equal to 1, Strabala, 2005), resulting in a number of granules used here varying between one and three for each day. For each 1 km by 1 km pixel in each such granule, that pixel is cloudy if both bit fields 2 and 3 are equal to 0, and clear otherwise (Strabala, 2005). A further test (not shown) where both "cloudy" and "uncertain clear" (bits 2 and 3 set to 00 and 01 respectively) were treated as cloudy yielded no significant difference. Finally, we interpolated the MYD35_L2 cloud mask onto the 5 km grid used by APP.

For APP, we consider that a pixel is clear if it matches all three criteria:

- T4 $\geqslant$ 245 K (Yamanouchi et al., 1987);
- $|T34| \leqslant$ 2 K (Yamanouchi et al., 1987);
- and 0 K $\leqslant$ T45 $\leqslant$ 2 K (Vincent, 2018; Vincent et al., 2008).

For all 90 000 pixels of each daily file, we determine where:

- both MYD35_L2 and APP detect no cloud (cyan on supp. Fig. A1d);
- both MYD35_L2 and APP detect a cloud (grey);
- MYD35_L2 detects no cloud but APP does (orange);
- MYD35_L2 detects a cloud but APP does not (black).

The case where MYD35_L2, used as reference here, detects a cloud but APP does not is problematic and is the one we want to minimise. Over the 17 years common to both products, restricting ourselves to the period 1 July - 31 October studied in this manuscript, this case happens on average to 19.1% of the pixels (supp. Table A1). The opposite case, where a clear pixel is wrongly detected as cloudy by APP and eliminated from the study, happens on average to 12.4% of the pixels (supp. Table A1).

We investigated the possible cause for these misdetections by randomly plotting and scrutinising individual days. We here present only one of them, 10 September 2014, as it is relatively easy to analyse even to the untrained eye (supp. Fig. A1). We

Table A1. For all years from 2002 to 2018, between 1 July and 31 October (dates of winter for polynya detection in this manuscript), median percentage of pixels: that are cloudy according to the reference cloud mask MYD35_L2 but were not detected by the criteria applied to APP (first column); that are clear in the reference, but were incorrectly detected as cloudy in APP (second column); which are detected in both products as clear or cloudy (third column). First line is when applying the original Yamanouchi et al. (1987) criterion $|T34| > 2$ K; second line, when modifying it as explained in this appendix.

	Cloudy in MYD35_L2	Cloudy in APP	Both agree
$\|T34\| > 2$ K	19.1%	12.4%	64.5%
$\|T34\| > 1.5$ K	14.4%	15.5%	67.4%

focused on the pixels where the reference is cloudy but APP is clear (black dots on supp. Fig. A1c and d). These pixels fall in two categories:

- they are on the edge of a cloud, and hence may have moved between the acquisition of MY35_L2 and that of APP;
- or they correspond to $|T34| > 1.5$ K (highlighted with yellow core on supp. Fig. A1d).

The first case cannot be further verified, as APP is composed of a mosaic of images acquired over a 6h window. For the second case however, we modified the criterion for cloud detection in APP from $|T34| > 2$ K (Yamanouchi et al., 1987) to $|T34| > 1.5$ K, and performed the comparison again. The improvement was significant, with "missed" pixels decreasing from 19.1% to 14.4% overall (supp. Table A1). The agreement between the two products even increased from 64.5% to 67.4%. By decreasing the T34 threshold we increased the sensitivity of APP, resulting unfortunately in an increase in the number of pixels wrongly detected as cloudy from 12.4% to 15.5%.

In conclusion, we apply throughout this paper the modified criteria for clear pixels:

- T4 $\geqslant$ 245 K (Yamanouchi et al., 1987);
- $|T34| \leqslant 1.5$ K (after Yamanouchi et al., 1987, and this appendix);
- and 0 K $\leqslant$ T45 $\leqslant$ 2 K (Vincent, 2018; Vincent et al., 2008).

For the entire period common to the two products, these criteria fail to detect 14.4% of the pixels as cloudy, but also wrongly detect 15.5% of the pixels as cloudy when they are clear. As these two values balance out and that they are, to some extent at least, caused by the difference in acquisition time of the two products, no further action is taken to estimate the accuracy of our results.

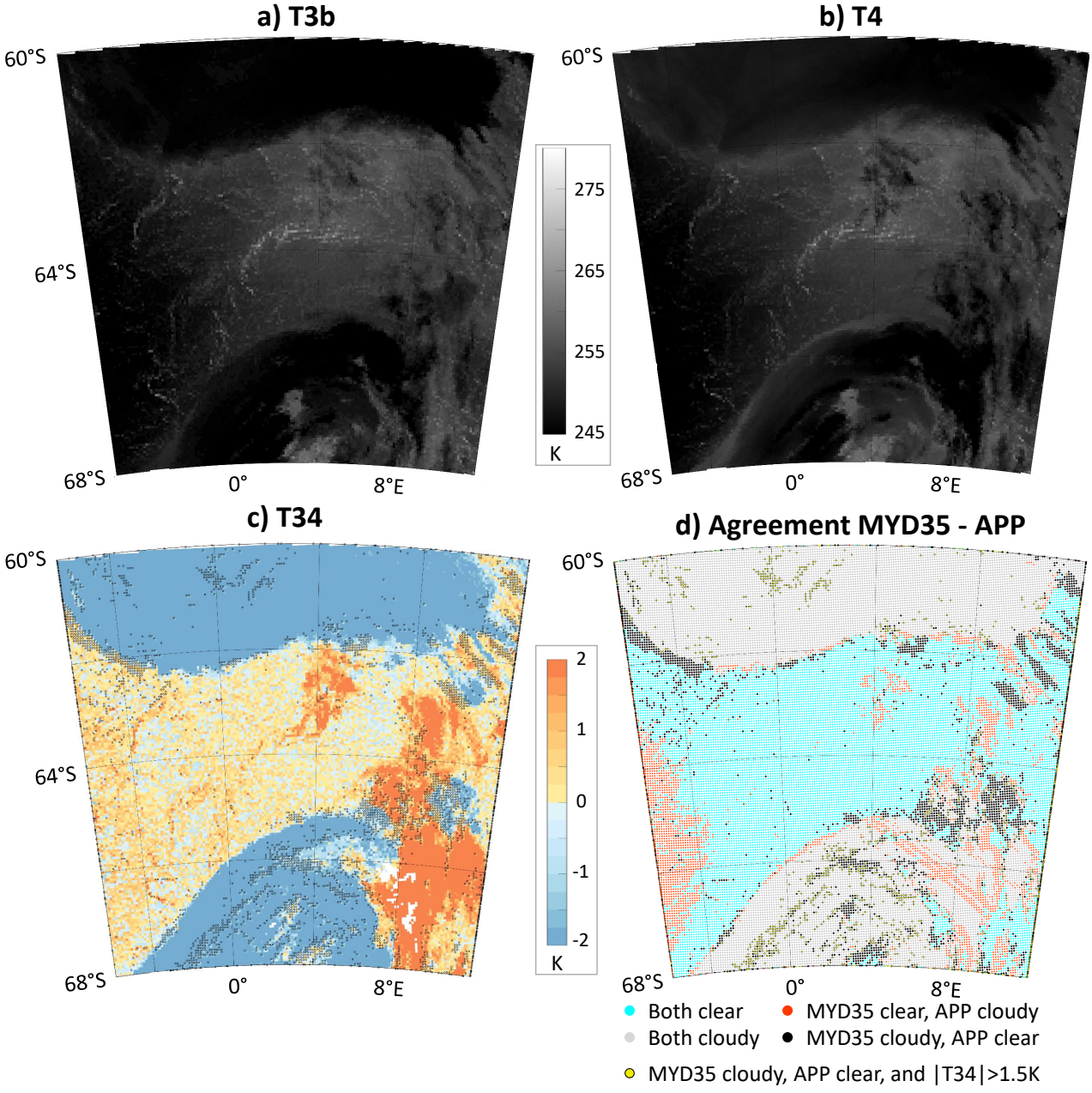

Figure A1. 10 September 2014. Infrared brightness temperatures T3b (a) and T4 (b), on the same colour scale, and their difference T34 (c). On these three panels, two large cloud systems are visible at the top and bottom (low T34), and smaller clouds to the right (large T34). Comparison of the cloud mask based on the APP data and the MYD35_L2 reference (d): cyan for light pixels in both, grey for cloudy pixels in both, orange for pixels clear in the MYD35_L2 reference but detected as cloudy with APP, and black for pixels cloudy in the reference but incorrectly detected as clear. These black pixels are also indicated on (c). A yellow core highlights these incorrect black pixels where the absolute value of T34 is larger than 1.5 K, i.e. that are correctly detected as cloudy when the threshold on T34 is lowered from 2 K to 1.5 K.

Appendix B: Supplementary tables and figures

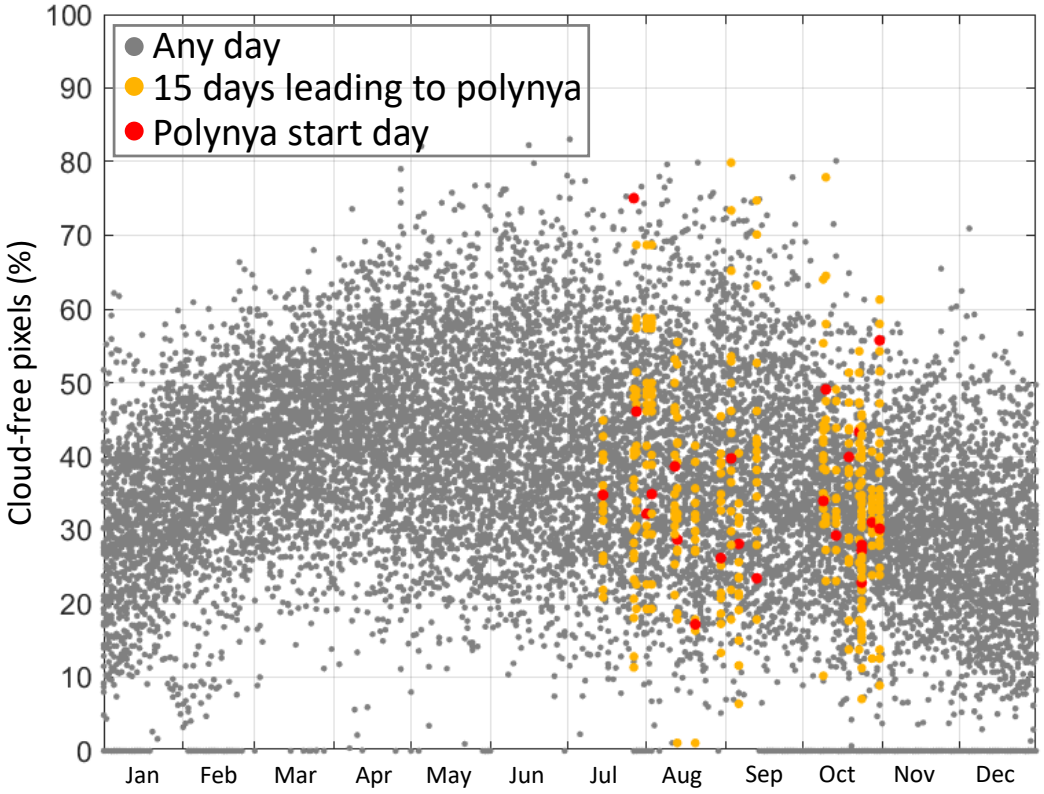

Figure B1. For each day of the year, percentage of cloud free pixels (out of 90000) for any year sampled by APP (grey), for the 15 days leading to a polynya event (orange), and the days a polynya opens (red).

Table B1. Characteristics of the events detected in section 3.1, with sea ice concentration < 60% criterion: start date, latitude (lat., in degree North) and longitude (lon., in degree East) of the centre, maximum area (in km^2) and duration (in days). The last two columns are the median percentage of cloud-free pixels (out of 90000) over the 15 days prior to the polynya opening, as well as the minimum-maximum interval of that percentage.

Start date	centre lat.	centre lon.	max. area	duration	cloud-free, median	cloud-free, min-max
17 July 1980	-63.9	2.2	5625	3	N/A	N/A
15 July 1991	-64.1	4.7	12500	5	34%	21-45%
24 Oct 1991	-63.7	5.1	5000	8	27%	16-41%
23 Oct 1992	-63.8	5.4	25625	9	23%	8-35%
13 Aug 1994	-63.7	3.2	21875	6	33%	2-56%
20 Aug 1994	-63.9	4.2	7500	5	30%	2-42%
6 Sept 1994	-64.0	5.0	18125	15	24%	7-41%
18 Oct 1996	-63.4	5.6	9375	11	38%	14-52%
22 Oct 1996	-63.7	3.7	9375	7	41%	14-55%
	-63.6	6.6	625	1		
30 Oct 1996	-63.4	5.6	625	1	43%	14-62%
27 July 1999	-67.7	-4.4	9375	1	30%	12-76%
	-66.6	-0.2	10000	2		
24 Oct 1999	-66.4	-0.2	14375	8	38%	18-46%
29 Aug 2000	-66.4	-1.3	21875	3	34%	14-46%
27 Oct 2000	-65.1	1.0	1250	2	32%	13-41%
30 Oct 2000	-65.2	1.8	6875	2	31%	9-36%
	-64.2	6.8	14375	2		
9 Oct 2004	-67.6	4.9	5000	4	39%	24-78%
	-63.8	5.7	8125	17		
13 Oct 2004	-67.5	2.0	4375	2	33%	24-50%
	-66.6	5.6	7500	2		
	-63.7	1.7	33125	14		
9 Oct 2005	-63.9	2.2	1875	2	40%	11-65%
27 July 2016	-64.2	6.5	2500	3	47%	20-69%
31 July 2016	-64.1	5.7	625	1	47%	20-69%
2 Aug 2016	-64.3	6.3	43125	8	47%	20-69%
11 Aug 2016	-65.0	3.9	17500	4	35%	22-54%
3 Sept 2017	-63.9	3.7	3125	5	42%	18-80%
13 Sept 2017	-64.3	4.2	71875	49	41%	18-75%

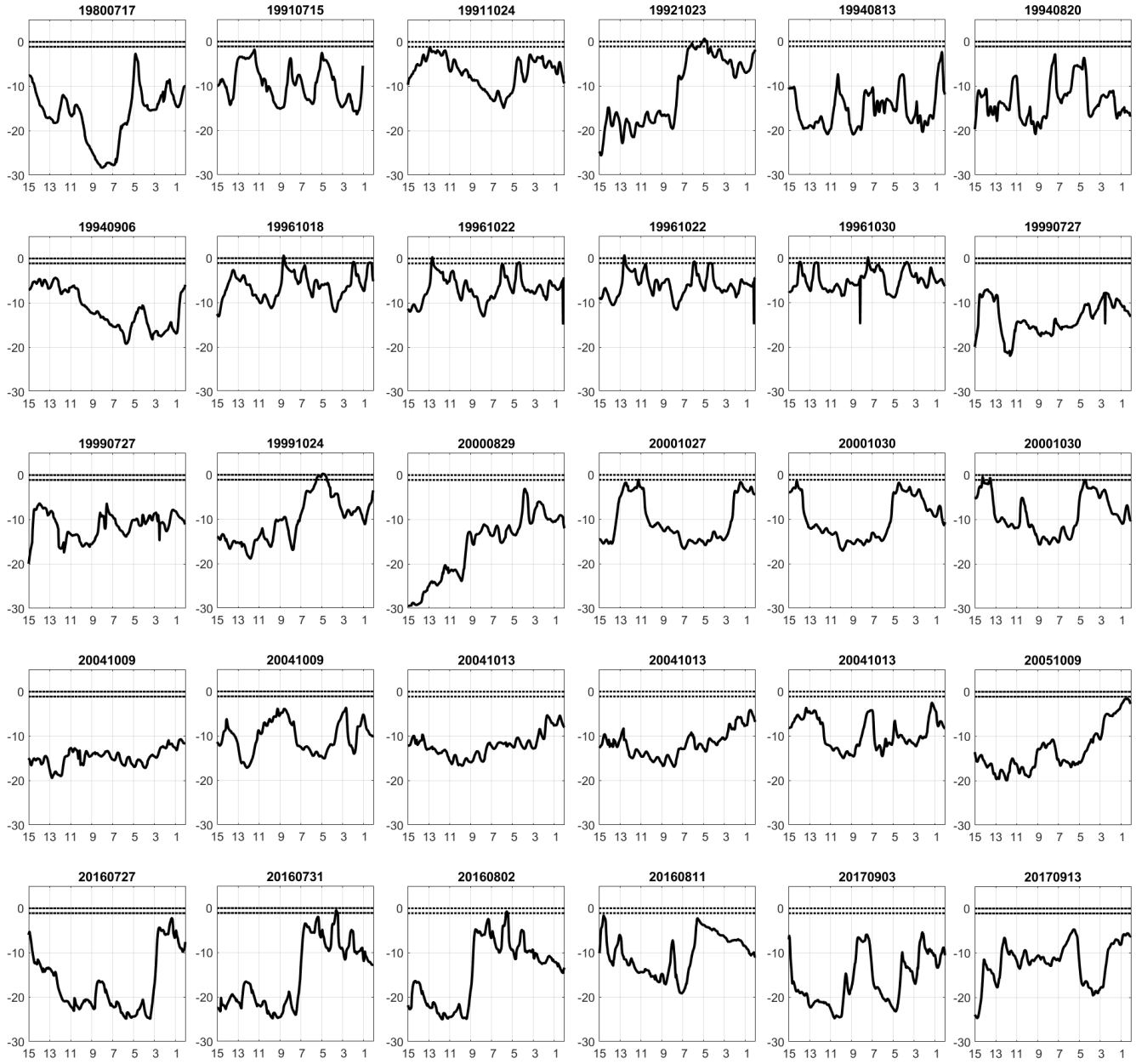

Figure B2. Time series of the 2 m air temperature at the location of the polynya, over the 15 days leading to the polynya event (date of the event in the panel title). x-axis: Days before the polynya event; y-axis: Air temperature in degree C. Horizontal dashed lines indicate the freezing temperature for young salty (-1.1 °C) or older fresh (0 °C) sea ice

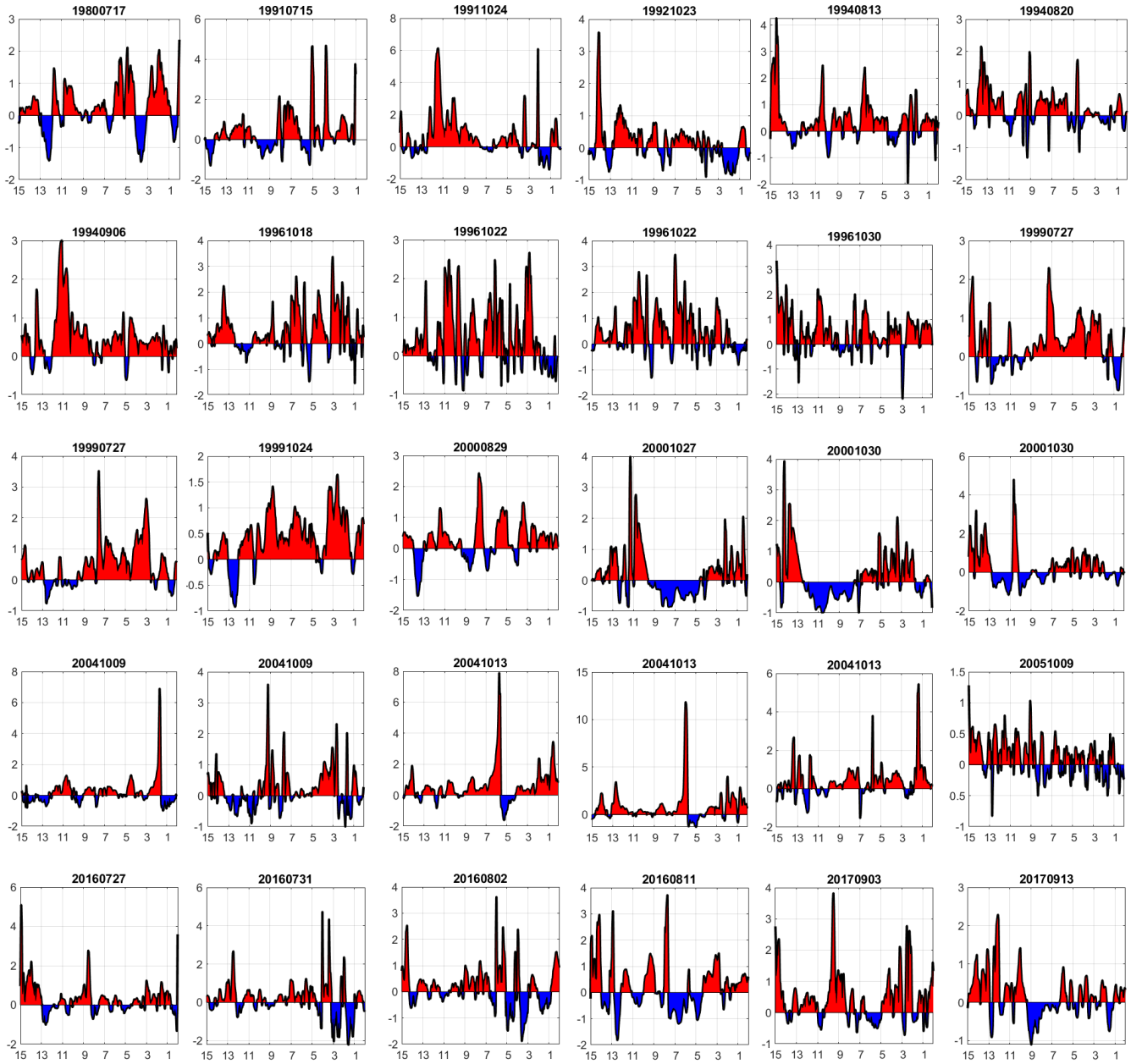

Figure B3. Time series of the curl of the wind at the location of the polynya, over the 15 days leading to the polynya event (date of the event in the panel title). x-axis: Days before the polynya event; y-axis: Curl of the wind as $\frac{\partial v}{\partial x} - \frac{\partial u}{\partial y}$, with the 10 m horizontal wind speeds u and v in ms^{-1} (see Methods). A positive curl (red) indicates divergence; negative (blue), the possibility of upwelling.

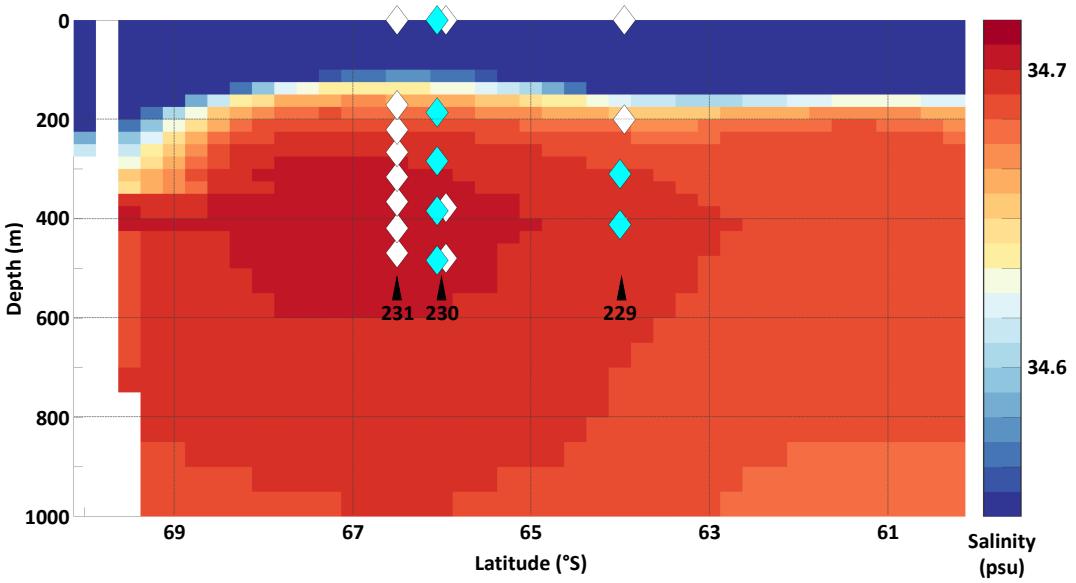

Figure B4. Climatological salinity along the Prime Meridian, from Zweng et al. (2018), showing the comparatively salty CDW in red. The diamonds indicate the location of the mooring sensors used for our analysis; for moorings 229 and 230, white indicates the older deployment (229-5, in 2002-2005, and 230-2, in 1999-2000) and cyan, the more recent one (229-13, in 2016-2019, and 230-4, 2002-2005); for mooring 231, only deployment 231-5 (2002-2005) could be used here.

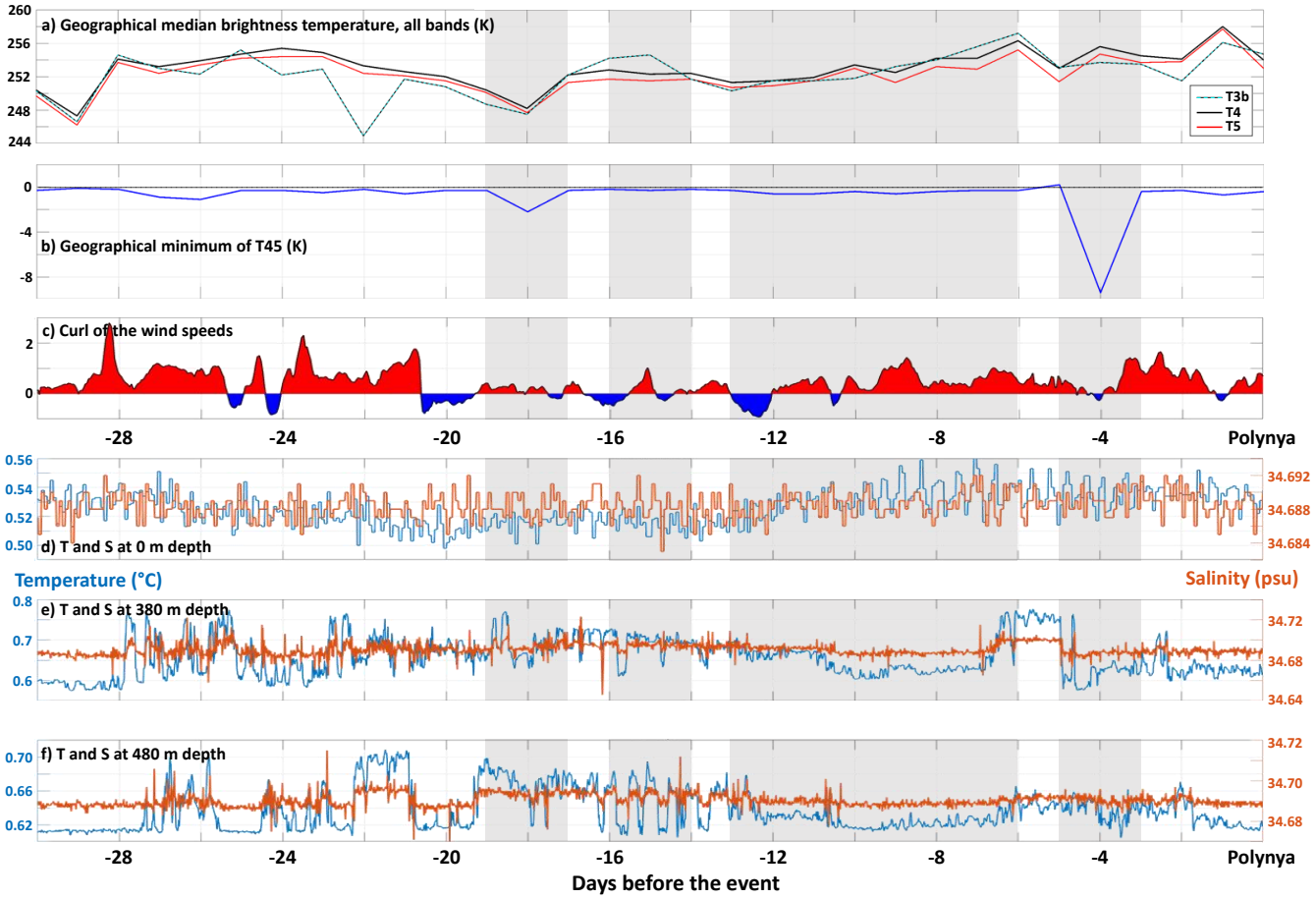

Figure B5. Conditions in the 30 days leading to the 24 October 1999 polynya. First, for the infrared criteria from section 3.2: a) geographical median over the polynya-prone region for the infrared brightness temperature band T3b (cyan), T4 (thick black) and T5 (red); b) geographical min over the polynya-prone region of the brightness temperature difference T45 (T4 minus T5). c) curl of the wind speeds as in supp Fig. B3. Finally, temperature (blue) and salinity (orange) timeseries from mooring 230-2 (see Fig. 8) at 0 (d), 380 (e) and 480 (f) m depth.

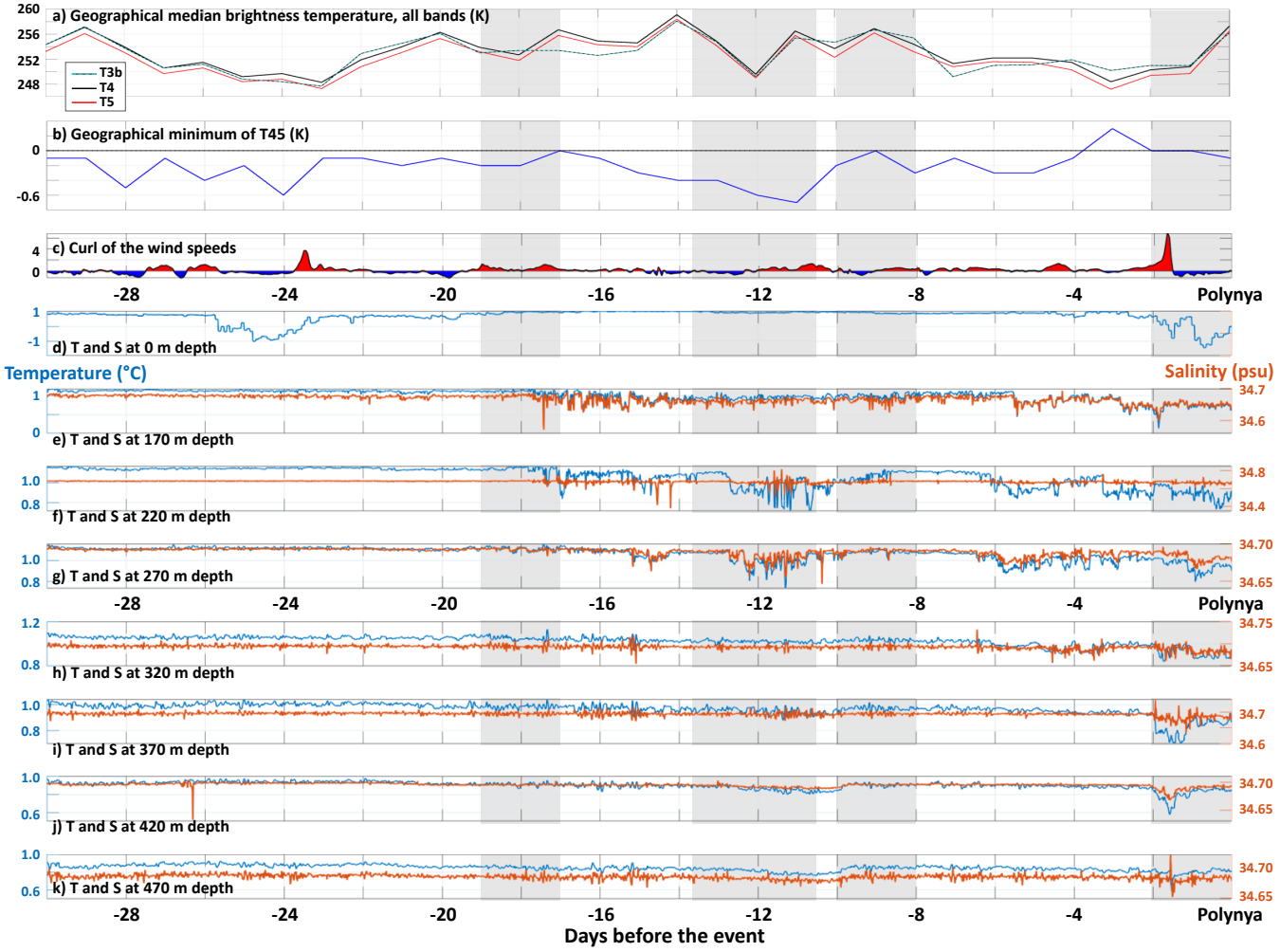

Figure B6. Conditions in the 30 days leading to the 9 October 2004 polynya. First, for the infrared criteria from section 3.2: a) geographical median over the polynya-prone region for the infrared brightness temperature band T3b (cyan), T4 (thick black) and T5 (red); b) geographical min over the polynya-prone region of the brightness temperature difference T45 (T4 minus T5). c) curl of the wind speeds as in supp Fig. B3. Finally, temperature (blue) and salinity (orange) timeseries from mooring 231-5 (see Fig. 8) at 0 (d), 170 (e), 220 (f), 270 (g), 320 (h), 370 (i), 420 (j) and 470 (k) m depth.

Author contributions. C.H. designed the study and conducted the Infrared and Mooring analysis. A.L. conducted the SAR analysis. Both authors contributed to the manuscript.

Competing interests. The authors declare no competing interest.

Acknowledgements. This project is funded by the Swedish National Space Agency (grant 164/18 awarded to C.H.). The authors thank Thomas Lavergne for his generous help while this idea was still at the proposal stage, and again, along with his colleagues at Metno, for their help with getting the data and eventually suggesting we use APP. We thank Julia Kukulies, Hui-Wen Lai and Martin Mohrmann for their help with the bit stripping script for the MYD35_L2 cloud masks. We also thank the two anonymous reviewers 1 and 3 and Stefan Kern (reviewer 2) for their comments that greatly improved the clarity and quality of this manuscript. Finally, C.H. is grateful to Le Chat for his unconditional support during these long working-from-home months.

References

Ackerman, S., P., M., R., F., and B., B.: MODIS Atmosphere L2 Cloud Mask Product. NASA MODIS Adaptive Processing System, Tech. rep., Goddard Space Flight Center, USA, available from http://dx.doi.org/10.5067/MODIS/MYD35_L2.006, 2017.

Aldenhoff, W., C., H., and Eriksson, L.: Comparison of ice/water classification in Fram Strait from C-and L-band SAR imagery, Annals of Glaciology, 59, 112–123, 2018.

Beckmann, A., Timmermann, R., Pereira, A. F., and Mohn, C.: The effect of flow at Maud Rise on the sea-ice cover–numerical experiments, Ocean Dynamics, 52, 11–25, 2001.

Cabré, A., Marinov, I., and Gnanadesikan, A.: Global atmospheric teleconnections and multidecadal climate oscillations driven by Southern Ocean convection, Journal of Climate, 30, 8107–8126, 2017.

Campbell, E., Wilson, E. A., Moore, G., Riser, S., Brayton, C. E., Mazloff, M., and Talley, L.: Antarctic offshore polynyas linked to Southern Hemisphere climate anomalies, Nature, 570, 319–325, 2019.

Carsey, F.: Microwave observation of the Weddell Polynya, Monthly Weather Review, 108, 2032–2044, 1980.

Cheon, W. and Gordon, A.: Open–ocean polynyas and deep convection in the Southern Ocean, Scientific reports, 9, 1–9, 2019.

Cheon, W., Park, Y., Toggweiler, J., and Lee, S.: The relationship of Weddell Polynya and open-ocean deep convection to the Southern Hemisphere westerlies, Journal of physical oceanography, 44, 694–713, 2014.

Cheon, W. G., Lee, S. K., Gordon, A. L., Liu, Y., Cho, C. B., and Park, J. J.: Replicating the 1970s' Weddell polynya using a coupled ocean-sea ice model with reanalysis surface flux fields, Geophysical Research Letters, 42, 5411–5418, 2015.

Comiso, J.: Satellite remote sensing of the Polar Oceans, Journal of Marine Systems, 2, 395–434, 1991.

Comiso, J. C.: Bootstrap Sea Ice Concentrations from Nimbus-7 SMMR and DMSP SSM/I-SSMIS, Version 3.1, Boulder, Colorado USA. NASA National Snow and Ice Data Center Distributed Active Archive Center, https://doi.org/10.5067/7Q8HCCWS4I0R, last accessed 8 November 2019, 2017.

de Steur, L., Holland, D., Muench, R., and McPhee, M.: The warm-water "Halo" around Maud Rise: Properties, dynamics and impact, Deep Sea Research Part I: Oceanographic Research Papers, 54, 871–896, 2007.

Demchev, D., Volkov, V., Kazakov, E., Alcantarilla, P. F., Sandven, S., and Khmeleva, V.: Sea ice drift tracking from sequential SAR images using accelerated-KAZE features, IEEE Transactions on Geoscience and Remote Sensing, 55, 5174–5184, 2017.

Drinkwater, M.: Satellite microwave radar observations of Antarctic sea ice. In Analysis of SAR data of the polar oceans, Springer, 1998.

Dufour, C. O., Morrison, A. K., Griffies, S. M., Frenger, I., Zanowski, H., and Winton, M.: Preconditioning of the Weddell Sea polynya by the ocean mesoscale and dense water overflows, Journal of Climate, 30, 7719–7737, 2017.

Fahrbach, E. and Rohardt, G.: Physical oceanography and current meter data from mooring AWI229-5, Alfred Wegener Institute, Helmholtz Centre for Polar and Marine Research, Bremerhaven, PANGAEA, https://doi.org/10.1594/PANGAEA.793018, 2012a.

Fahrbach, E. and Rohardt, G.: Physical oceanography and current meter data from mooring AWI230-2, Alfred Wegener Institute, Helmholtz Centre for Polar and Marine Research, Bremerhaven, PANGAEA, https://doi.org/10.1594/PANGAEA.793080, 2012b.

Fahrbach, E. and Rohardt, G.: Physical oceanography and current meter data from mooring AWI230-4, Alfred Wegener Institute, Helmholtz Centre for Polar and Marine Research, Bremerhaven, PANGAEA, https://doi.org/10.1594/PANGAEA.793082, 2012c.

Fahrbach, E. and Rohardt, G.: Physical oceanography and current meter data from mooring AWI231-5, Alfred Wegener Institute, Helmholtz Centre for Polar and Marine Research, Bremerhaven, PANGAEA, https://doi.org/10.1594/PANGAEA.793089, 2012d.

Francis, D., Eayrs, C., Cuesta, J., and Holland, D.: Polar cyclones at the origin of the reoccurrence of the Maud Rise Polynya in austral winter 2017, Journal of Geophysical Research: Atmospheres, 124, 5251–5267, 2019.

Francis, D., Mattingly, K. S., Temimi, M., Massom, R., and Heil, P.: On the crucial role of atmospheric rivers in the two major Weddell Polynya events in 1973 and 2017 in Antarctica, Science advances, 6, eabc2695, 2020.

GEBCO Compilation Group: GEBCO 2019 Grid, https://doi.org/10.5285/836f016a-33be-6ddc-e053-6c86abc0788e, 2019.

Gloersen, P., Campbell, W., Cavalieri, D., Comiso, J., Parkinson, C., and Zwally, H.: Arctic and Antarctic sea ice, 1978–1987, Satellite Passive-Microwave Observations and Analysis, 290, 1992.

Gordon, A.: Deep Antarctic convection west of Maud Rise, Journal of Physical Oceanography, 8, 600–612, 1978.

Gordon, A., Visbeck, M., and Comiso, J.: A possible link between the Weddell Polynya and the Southern Annular Mode, Journal of Climate, 20, 2558–2571, 2007.

Heuzé, C. and Aldenhoff, W.: Near-Real Time Detection of the Re-Opening of the Weddell Polynya, Antarctica, from Spaceborne Infrared Imagery, IGARSS 2018-2018 IEEE International Geoscience and Remote Sensing Symposium, pp. 5613–5616, 2018.

Heuzé, C., Heywood, K., Stevens, D., and Ridley, J.: Changes in global ocean bottom properties and volume transports in CMIP5 models under climate change scenarios, Journal of Climate, 28, 2917–2944, 2015a.

Heuzé, C., Ridley, J., Calvert, D., Stevens, D., and Heywood, K.: Increasing vertical mixing to reduce Southern Ocean deep convection in NEMO3.4, Geoscientific Model Development, 8, 3119–3130, 2015b.

Hirano, D., Fukamachi, Y., Watanabe, E., Ohshima, K., Iwamoto, K., Mahoney, A., Eicken, H., Simizu, S., and Tamura, T.: A wind-driven, hybrid latent and sensible heat coastal polynya off Barrow, Alaska, Journal of Geophysical Research: Oceans, 121, 980–997, 2016.

Holland, D. M.: Explaining the Weddell Polynya–a large ocean eddy shed at Maud Rise, Science, 292, 1697–1700, 2001.

IOC, SCOR and IAPSO: The international thermodynamic equation of seawater - 2010: Calculation and use of thermodynamic properties, Tech. rep., UNESCO, available from http://www.TEOS-10.org, 2010.

Key, J. and Barry, R.: Cloud cover analysis with Arctic AVHRR data: 1. Cloud detection, Journal of Geophysical Research: Atmospheres, 94, 18 521–18 535, 1989.

Key, J., Liu, Y., Wang, X., and NOAA CDR Program: NOAA Climate Data Record (CDR) of AVHRR Polar Pathfinder (APP) Cryosphere, Version 2.0, NOAA National Centers for Environmental Information (NCEI), https://doi.org/10.25921/X2X1-JR34, last accessed 15 January 2020, 2019.

Kjellsson, J., Holland, P., Marshall, G., Mathiot, P., Aksenov, Y., Coward, A., Bacon, S., Megann, A., and Ridley, J.: Model sensitivity of the Weddell and Ross seas, Antarctica, to vertical mixing and freshwater forcing, Ocean Modelling, 94, 141–152, 2015.

Lindsay, R., Holland, D., and Woodgate, R.: Halo of low ice concentration observed over the Maud Rise seamount, Geophysical research letters, 31, 2004.

Locarnini, R., Mishonov, A., Baranova, O., Boyer, T., Zweng, M., Garcia, H., Reagan, J., Seidov, D., Weathers, K., Paver, C., and Smolyar, I.: World Ocean Atlas 2018, Volume 1: Temperature, A. Mishonov Technical Ed.; NOAA Atlas NESDIS 81, 2018.

Ludwig, V., Spreen, G., Haas, C., Istomina, L., Kauker, F., and Murashkin, D.: The 2018 North Greenland polynya observed by a newly introduced merged optical and passive microwave sea-ice concentration dataset, The Cryosphere, 13, 2019.

Mäkynen, M., Kern, S., Rösel, A., and Pedersen, L.: On the estimation of melt pond fraction on the Arctic Sea ice with ENVISAT WSM images, IEEE Transactions on Geoscience and Remote Sensing, 52, 7366–7379, 2014.

Marshall, J. and Plumb, R. A.: Atmosphere, ocean and climate dynamics: an introductory text, Academic Press, 2016.

Martin, S. and Cavalieri, D.: Contributions of the Siberian shelf polynyas to the Arctic Ocean intermediate and deep water, Journal of Geophysical Research: Oceans, 94, 12 725–12 738, 1989.

Martin, T., Park, W., and Latif, M.: Multi-centennial variability controlled by Southern Ocean convection in the Kiel Climate Model, Climate dynamics, 40, 2005–2022, 2013.

Maslanik, J. A., Fowler, C., Stroeve, J., Drobot, S., Zwally, J., Yi, D., and Emery, W.: A younger, thinner Arctic ice cover: Increased potential for rapid, extensive sea-ice loss, Geophysical Research Letters, 34, L24 501, 2007.

Meier et al., W.: Arctic sea ice in transformation: A review of recent observed changes and impacts on biology and human activity, Reviews of Geophysics, 52, 185–217, 2014.

Mohrmann, M., Heuzé, C., and Swart, S.: Southern Ocean polynyas in CMIP6 models, The Cryosphere Discussion, discussion open, https://doi.org/10.5194/tc-2021-23, 2021.

Morales Maqueda, M., Willmott, A., and Biggs, N.: Polynya dynamics: A review of observations and modeling, Reviews of Geophysics, 42, 2004.

Murashkin, D., Spreen, G., Huntemann, M., and Dierking, W.: Method for detection of leads from Sentinel-1 SAR images, Annals of Glaciology, 59, 124–136, 2018.

Nandan, V., Geldsetzer, T., Yackel, J., Mahmud, M., Scharien, R., Howell, S., King, J., Ricker, R., and Else, B.: Effect of snow salinity on CryoSat-2 Arctic first-year sea ice freeboard measurement, Geophysical Research Letter, 44, 10–419, 2017.

Notz, D. and Stroeve, J.: Observed Arctic sea-ice loss directly follows anthropogenic CO2 emission, Science, 354, 747–750, 2016.

Petty, A., Hutchings, J., Richter-Menge, J., and Tschudi, M.: Sea ice circulation around the Beaufort Gyre: The changing role of wind forcing and the sea ice state, Journal of Geophysical Research: Oceans, 121, 3278–3296, 2016.

Preußer, A., Heinemann, G., Willmes, S., and Paul, S.: Sea ice circulation around the Beaufort Gyre: The changing role of wind forcing and the sea ice state, Multi-decadal variability of polynya characteristics and ice production in the North Water Polynya by means of passive microwave and thermal infrared satellite imagery, 7, 15 844–15 867, 2015.

Randall-Goodwin, E., Meredith, M., Jenkins, A., Yager, P., Sherrell, R., Abrahamsen, E., Guerrero, R., Yuan, X., Mortlock, R., Gavahan, K., and Alderkamp, A.: Freshwater distributions and water mass structure in the Amundsen Sea Polynya region, Antarctica, Elementa: Science of the Anthropocene, 3, 2015.

Rohardt, G. and Boebel, O.: Physical oceanography and current meter data from mooring AWI229-13, Alfred Wegener Institute, Helmholtz Centre for Polar and Marine Research, Bremerhaven, PANGAEA, https://doi.org/10.1594/PANGAEA.898781, 2019.

Saunders, R. W. and Kriebel, K. T.: An improved method for detecting clear sky and cloudy radiances from AVHRR data, International Journal of Remote Sensing, 9, 123–150, 1988.

Schillat, M., Jensen, M., Vereda, M., Sánchez, R. A., and Roura, R.: Tourism in Antarctica: A multidisciplinary view of new activities carried out on the white continent, Springer, 2016.

Smedsrud, L.: Warming of the deep water in the Weddell Sea along the Greenwich meridian: 1977–2001, Deep Sea Research Part I: Oceanographic Research Papers, 52, 241–258, 2005.

Smith Jr, W. O., , and Barber, D.: Polynyas: Windows to the world, Elsevier, 2007.

Spreen, G., Kaleschke, L., and Heygster, G.: Sea ice remote sensing using AMSR-E 89-GHz channels , Journal of Geophysical Research: Oceans, 113, 2008.

Stocker et al., T. F.: Climate change 2013: the physical science basis. Contribution of working group I to the fifth assessment report of IPCC the intergovernmental panel on climate change, Cambridge University Press, 2014.

Strabala, K.: MODIS cloud mask user's guide, University of Wisconsin–Madison, 2005.

Swart et al., S.: Return of the Maud Rise polynya: Climate litmus or seaice anomaly? [in"State of the Climate in 2017"], Bulletin of the American Meteorological Society, 99, S188–S189, 2018.

Timmermann, R., Lemke, P., and Kottmeier, C.: Formation and maintenance of a polynya in the Weddell Sea, Journal of physical oceanography, 29, 1251–1264, 1999.

Vincent, R.: The effect of Arctic dust on the retrieval of satellite derived sea and ice surface temperatures, Scientific reports, 8, 2018.

Vincent, R., Marsden, R., Minnett, P., and Buckley, J.: Arctic waters and marginal ice zones: 2. An investigation of arctic atmospheric infrared absorption for advanced very high resolution radiometer sea surface temperature estimates, Journal of Geophysical Research: Oceans, 113, 2008.

von Schuckmann et al., K.: Copernicus Marine Service Ocean State Report, Issue 3, Journal of Operational Oceanography, 12, S1–S123, 2019.

Wilson, E., Riser, S., Campbell, E. C., and Wong, A.: Winter upper-ocean stability and ice–ocean feedbacks in the sea ice–covered Southern Ocean, Journal of Physical Oceanography, 49, 1099–1117, 2019.

Yamanouchi, T., Suzuki, K., and Kawaguchi, S.: Detection of clouds in Antarctica from infrared multispectral data of AVHRR, Journal of the Meteorological Society of Japan. Ser. II, 65, 949–962, 1987.

Zanowski, H., Hallberg, R., and Sarmiento, J.: Abyssal ocean warming and salinification after Weddell polynyas in the GFDL CM2G coupled climate model, Journal of Physical Oceanography, 45, 2755–2772, 2015.

Zhang, X., Dierking, W., Zhang, J., Meng, J., and Lang, H.: Retrieval of the thickness of undeformed sea ice from simulated C-band compact polarimetric SAR images, The Cryosphere, 10, 1529–1545, 2016.

Zweng, M., Reagan, J., Seidov, D., Boyer, T., Locarnini, R., Garcia, H., Mishonov, A., Baranova, O., Weathers, K., Paver, C., and Smolyar, I.: World Ocean Atlas 2018, Volume 2: Salinity, A. Mishonov Technical Ed.; NOAA Atlas NESDIS 82, 2018.